The Influence of Subsurface Conditions on the Spatial and Temporal Variability of Tropical SST and Rainfall in CFSv2 Reforecasts

Ravi P. Shukla[1] (ID)

[1]Center for Ocean-Land-Atmosphere Studies, George Mason University, Fairfax, VA, USA

Abstract This study examines the potential impact of subsurface potential temperature and current conditions on the sea surface temperature (SST) and rainfall over the tropical region using Climate Forecast System Version 2 (CFSv2) ensemble seasonal reforecasts for 1958–2014. The climatological difference of earlier period (1958–78; P58-78) and later period (1994–2014; P94-14) in January initialized reforecasts (JIR) depicts mild-warm SST over the equatorial eastern Pacific in January, but its magnitude becomes larger over there from May to August. The difference between JIR P58-78 and P94-14 depicts warm potential temperature (PT) up to 3°C over the equatorial central and eastern Pacific at depth from 155 to 70 m in January therefore 20°C isotherm of JIR P58-78 in January tends to be deeper in the equatorial eastern Pacific than JIR P94-14. The magnitude of equatorial undercurrent (EUC) in JIR P58-78 is larger in the eastern Pacific at depth from 125 to 35 m from January to February than JIR P94-14. Therefore, water upwelled to the surface through EUC was usually warm in January of JIR P58-78. As lead months increase, the center of warm PT gradually moves upward in the eastern Pacific than its location in January, resulting in development of warm SST in the eastern Pacific in March. The difference between April initialized reforecasts P58-78 and P94-14 depicts warm PT up to 1.5°C in the eastern Pacific at depth from 135 to 35 m in April but as lead months increase, magnitude of warm PT gradually decreases, resulting in negligible difference SST over the eastern Pacific.

1. Introduction

The El Niño–Southern Oscillation (ENSO) is a result of slowly varying interactions between the tropical-ocean and atmosphere, including wave propagation in the upper-ocean and shifts in the major zones of convection in the atmosphere (Bjerknes, 1969; McPhaden, 2004, 2015; Neelin et al., 1998; Wallace et al., 1998; Wyrtki, 1975). Many previous studies have already shown that the sea surface temperature (SST) variations associated with ENSO provide an important source of predictability that can be exploited for seasonal to interannual time scales climate forecasting for precipitation and large-scale atmospheric circulation and other variables over the continental United States in winter and summer, and over Asia primarily in summer (Adams & Comrie, 1997; Higgins et al., 1999; Lau & Nath, 2000; Ropelewski & Halpert, 1986; Shukla & Paolin, 1983; Shukla & Huang, 2015; Webster & Yang, 1992). Seasonal climate predictions are important information for practitioners in fields such as agriculture, energy, fisheries, food security, and water resource management. Understanding the dynamics of the equatorial Pacific Ocean and improving predictions of ENSO, therefore, is a vital goal of current research and development in this area.

Extensive previous studies during the past decades have used conceptual models to describe the nature of the ENSO variability in the tropical Pacific (Battisti, 1988; Bjerknes, 1969; Cane & Zebiak, 1985; Jin, 1997a, 1997b; Neelin et al., 1998; Schopf & Suarez, 1988; Suarez & Schopf, 1988; Sun, 2003; Wyrtki, 1975, 1985). Using proxy measurements and numerical simulations, many studies explored the relationship between variability in heat content in the tropical Pacific and ENSO cycle (Cane & Zebiak, 1985; McPhaden, 1999; McPhaden et al., 1998; Wyrtki, 1985). According to the "delayed oscillator" theory (Battisti & Hirst, 1989; Schopf & Suarez, 1988; Suarez & Schopf, 1988), the equatorial ocean wave processes and the coupling between the ocean and atmosphere govern the development and decay of the ENSO cycle. According to the "recharge oscillator" paradigm (Jin, 1997a, 1997b), changes in the equatorial western Pacific thermocline depth are related to the timing of El Niño and La Niña events. The SST anomaly over the equatorial eastern Pacific is regulated by upwelling and thermocline feedback processes. The "recharge oscillator" hypothesis is

consistent with the "delayed oscillator" (Battisti & Hirst, 1989; Schopf & Suarez, 1988; Suarez & Schopf, 1988) near the bifurcation point but emphasizes meridional mass transports rather than equatorial wave dynamics.

Many systematic biases and uncertainties persist in the state-of-the-art coupled general circulation models (CGCMs) so that simulations are less accurate and seasonal forecasts have lower prediction skill of ENSO (Deser et al., 2006; Huang, Shin, et al., 2017; Large & Danabasoglu, 2006; Shukla & Huang, 2015; Wittenberg et al., 2006; Yeager et al., 2006; Zhang et al., 2009; Zhu et al., 2012). Large and Danabasoglu (2006) demonstrated that the Community Climate System Model version 3 (CCSM3; T31x3 configuration) simulation depicts the maximum mean zonal speed of Equatorial Undercurrent (EUC) is around 80 cm/s, whereas it is around 100 cm/s in the observations (Johnson et al., 2002). However, they also reported that the South Equatorial Current (SEC) is generally confined too deep in the eastern half of the Pacific in both coupled and uncoupled simulation compared to observations, and similar features are also found in the high-resolution ocean simulation (Large & Danabasoglu, 2006). Wittenberg et al. (2006) demonstrated that the Geophysical Fluid Dynamics Laboratory (GFDL) coupled Climate Model Versions 2.1 (CM2.1) simulations depict the maximum mean zonal speed of the EUC is around 90 cm/s. Using the Hybrid Coordinate Ocean Model (HYCOM) simulation, Shaji et al. (2005) reported maximum core velocity of the EUC in February is 80 cm/s at 140°W at a depth of about 120 m.

Many previous studies have used the coupled land-atmospheric-ocean model, the National Centers for Environmental Prediction (NCEP) Coupled Forecast System Version 2 (CFSv2; Saha et al., 2014) to evaluate the seasonal prediction and prediction of the ENSO, Indian summer monsoon (ISM), and others the important process of atmosphere and ocean in the reforecasts and long-term simulations (Huang, Shin, et al., 2017; Kim et al., 2012; Shin et al., 2019; Shukla et al., 2017; Shukla, Huang, Dirmeyer, & Kinter, 2019; Shukla, Huang, Dirmeyer, Kinter, Shin, et al., 2019; Shukla & Huang, 2020; Shukla & Shin, 2020; Zhu et al., 2012; Zhu & Shukla, 2013, and papers cited therein). Zhu and Shukla (2013) demonstrated that the atmospheric model produces higher rainfall biases and unrealistic interannual variability in reforecasts over the Asia-Pacific region, suggesting that a coupled CFSv2 is necessary for prediction of rainfall over there. There are several systematic errors in the CFSv2 simulation and reforecasts. For example, the cold bias in the tropic Pacific SST and enhance cold bias in the upper tropical atmosphere (Shukla & Huang, 2015). The ENSO is overly active in CFSv2 simulation during and before the Asian summer monsoon season and persists for a longer period in comparison to the observed (Shukla & Huang, 2015). Ramu et al. (2016) compared simulation and prediction skill of ISM between horizontal resolutions T126 and T382 using CFSv2 seasonal reforecasts for periods 1981–2008. They found that CFSv2 depicts some systematic biases at both resolutions but simulation of ISM mean state in better in the high-resolution run. In another study, Ramu et al. (2017) found that high-resolution model can predict ISM rainfall reasonable at a lead time of 3–4 months. Shin et al. (2019) demonstrated the ISM predictability has different characteristics in different phases of the ENSO cycle, and predictability of precipitation over the Asia-Pacific region is higher during the summer immediately after a major ENSO event. Zhu et al. (2012) compared the impact of four ocean initial conditions (ICs) on the prediction skill in the tropical Pacific Ocean using a coupled CFSv2 model for 1979–2008 and found the European Centre for Medium Range Weather Forecasts (ECMWF) NEMO variational ocean data assimilation system (Mogensen et al., 2012) based analysis produce better prediction skill of ENSO among a group of ocean reanalysis data sets. Using 57-year (1958–2014) CFSv2 reforecasts, Huang, Shin, et al. (2017) demonstrated that prediction skill of SST anomalies is lower over the North Pacific and North Atlantic before 1979 but prediction skill of onset and development of ENSO events in 1958–1978 is comparable to that for 1979–2014 although the skill of the earlier predictions declines faster for the ENSO decay. Using 58-year (1958–2015) CFSv2 April initialized reforecasts, Shukla and Shin (2020) demonstrated that spread among ensemble members within a certain range is one of the important factors for improving summer rainfall prediction skill over Indian landmass in the seasonal reforecasts. Chowdary et al. (2016) found that CFSv2 depicts warm subsurface bias between 150- and 200-m in the tropical Indian Ocean, it may due to strong vertical shear in horizontal currents in the model, resulting in deeper penetration of the warm waters.

Goswami et al. (2016) found that coupled CFSv2 depicts cold SST bias over the northern Indian Ocean and biases in the vertical thermal structure along the equator in the India Ocean, and longitudinally along the Bay of Bengal. The high-resolution and high-frequency observation over the Bay of Bengal may improve

the ISM forecasts. Samanta et al. (2018) found that CFSv2 is not able to simulate warm SST front over the coastal Bay of Bengal that is necessary for central ISM rainfall.

In this study, I have explored the impact of the subsurface potential temperature and current conditions over the equatorial central Pacific Ocean on the mean state of SST and rainfall over the tropical region in the NCEP CFSv2 seasonal reforecasts. For this purpose, I have analyzed a set of 20-member ensemble CFSv2 (Saha et al., 2014) seasonal reforecasts for the period 1958–2014, which is initialized in January and April (Huang, Shin, et al., 2017). As mentioned in section 2 that ocean initial conditions (OICs) were taken from instantaneous restart files of the ECMWF Ocean Reanalysis System 4 (ORAS4; Balmaseda et al., 2013) for the whole period 1958–2014 but it may assume that the quality of potential temperature and current conditions in ORAS4 is different before and after 1979; therefore, I have defined two time periods of 21 years in January initialized reforecasts (JIR) and April initialized reforecasts (AprIR), the earlier period (1958–1978; hereafter P58-78) and later period (1994–2014; hereafter P94-14) in order to examine the potential impact of subsurface potential temperature and current conditions, and its association to SST and rainfall over the tropical Pacific during summer. The difference between JIR P58-78 and P94-14 depicts mild-warm SST over the equatorial central Pacific in January but its magnitude becomes larger and expanding farther to the eastern Pacific from May to August. A possible mechanism for warmer SST over the equatorial eastern Pacific during summer will be explored in section 4.

The land ICs and atmosphere ICs were taken from several different data sources before and after 1979 in the seasonal reforecasts for the period 1958–2014 (Huang, Shin, et al., 2017), and their impacts will discuss in a separate paper (Shukla, 2020, under review).

The remainder of this paper is organized as follows. Section 2 briefly describes the model, the experimental design, and verification data sets. Section 3 presents the mean summer state in the earlier period (P58-78) and later period (P94-14) in both JIR and AprIR. Section 4 depicts the impact of subsurface OICs on the spatial and temporal variability of SST and rainfall in both JIR and AprIR. A summary and discussion are given in section 5.

2. Model Description, Experimental Design, and Observational Data Sets

The CGCM used in this study is NCEP CFSv2 (Saha et al., 2014) that includes the atmospheric model, which has a spectral horizontal resolution of T126 (105-km grid spacing) and 64 vertical levels in a hybrid sigma-pressure coordinate, and oceanic model (Geophysical Fluid Dynamics Laboratory Modular Ocean Model version (MOM4); Griffies et al., 2004), and sea ice (Winton, 2000), and land model (Noah land surface model; Ek et al., 2003). The MOM4 is configured for the global ocean with a horizontal grid of $0.5° × 0.5°$ poleward of 30°S/30°N and meridional resolution increasing gradually to 0.25° between 10°S and 10°N. Vertically, it has 40 levels in a z coordinate, with 27 levels within the upper 400 m and the maximum depth at approximately 4.5 km. In this study, a revised version of coupled CFSv2 was used that eliminated a code inconsistency at the air-sea interface and adjusted parameters for sea ice albedo to maintain realistic multi-year sea ice cover in the Arctic Ocean (Huang et al., 2015). Details of JIR and AprIR are described in Huang, Thorne, et al. (2017). In brief, the OICs were taken from five instantaneous restart files of ECMWF ORAS4 for the whole period 1958–2014 (Balmaseda et al., 2013). Since 1979, the land, atmosphere, and sea ice ICs were taken from the Climate Forecast System Reanalysis (CFSR; Saha et al., 2010). For the period 1958–1978, the atmospheric ICs were taken from the ERA-40 reanalysis (Uppala et al., 2005) and the land ICs were taken from the reprocessed 3-hourly National Aeronautics and Space Administration (NASA) Global Land Data Assimilation System, Version 2.0 (GLDAS-2.0) analysis on a $1° × 1°$ (Rodell et al., 2004; Rui & Beaudoing, 2015). An ensemble reforecast of 20 members is generated by matching each of the five ocean ICs at 00Z first of January and April with the atmospheric and land ICs at 00Z of the first 4 days of January and April. All the results discussed in this paper are based on mean of 20-ensemble members in both JIR and AprIR. I have chosen JIR because the ENSO events typically peak in strength in January, and the influence of ENSO is strongest at that time in the western Pacific Ocean, continental United States and maritime continent. On the other hand, reforecasts initialized in April depict lower prediction skills of ENSO in comparison to reforecasts initialized in other seasons due to the effect of the spring predictability barrier.

The observed SST used for verification is the global monthly Extended Reconstructed SST, Version 5 (ERSSTv5; Huang, Thorne, et al., 2017) for 1958–2015 on a $2° × 2°$ grid. Monthly World Ocean Atlas 2009

(WOA09) in situ temperature (Locarnini et al., 2010) and salinity (Antonov et al., 2010) at $1° \times 1°$ is used in this study. For verification the model output, I have calculated monthly climatology of three-dimensional oceanic potential temperature, zonal currents, and salinity from NCEP CFSR (Saha et al., 2010), NCEP GODAS (Behringer, 2005), ECMWF Ocean Reanalysis System 3 (ORA-S3; Balmaseda et al., 2008), and ECMWF Comprehensive Modeling of the Earth System for Better Climate Prediction and Projection (COMBINE-NV; Balmaseda et al., 2013) for the period 1979–2008. Monthly gridded Global Precipitation Climatology Project (GPCP v2.2; Adler et al., 2003) at a grid resolution of $2.5° \times 2.5°$ longitude for the period 1979–2015 is used in this study. The India Meteorological Department (IMD) gridded rainfall data at $0.25° \times 0.25°$ grid used for the period 1958–2015 (Pai et al., 2013). I have also performed calculations for two additional cases, (i) earlier period (1958–1968) and later period (2004–2014), and (ii) earlier period (1958–1978) and later period (1979–2014). It is found that qualitatively the spatial structures of the climatological difference of variables in both cases (i) and (ii) (results not shown) are similar as discussed in the manuscript.

3. Sensitivity of Mean Summer State to Initialization Periods of Reforecasts

To explore the impact of OICs quality (e.g., potential temperature and zonal current) on the spatial and temporal variability of SST and rainfall over the tropical region in seasonal reforecasts, monthly climatology of several variables have calculated for the earlier period (P58-78) and later period (P94-14) in both JIR and AprIR. Figure 1 depicts the climatological difference of SST between JIR P58-78 and P94-14 in January (Figure 1a), May (Figure 1b), mean of June–July (JJ; Figure 1c), and mean of August–September (AS; Figure 1d). The SST is generally cooler over the northwestern Pacific and the northern Atlantic Ocean in January (Figure 1a), May (Figure 1b), and JJ (Figure 1c). The cold SST difference in the northern western Pacific and northern Atlantic Ocean is an extension of the cold skin temperature from the continent (Shukla, 2020, under review; Shukla, Huang, Dirmeyer, Kinter, Shin, et al., 2019; Shukla & Huang, 2020). The climatological difference between JIR P58-78 and P94-14 depicts warm SST over the equatorial central Pacific mainly between 2°S and 2°N, 150–130°W up to 0.6°C in January (Figure 1a). The magnitude of warm SST in the difference between JIR P58-78 and P94-14 becomes larger over the tropical Pacific and expanding farther to the eastern Pacific during May (Figure 1b) and JJ (Figure 1c) in comparison to its location in January (Figure 1a). It implies that the earlier period is warmer than the later period over the equatorial tropical Pacific from May to September in JIR. The annual value of the NINO3.4 SST index in January, July, and September displays in Figures 1e–1g respectively that is defined as averaged SST over 5°S to 5°N and 120–170°W. A systematic shift in predicted monthly NINO3.4 SST index is found from January to September before and after 1979 (Figures 1e–1g). The interannual standard deviation (ISD) of January NINO3.4 SST index for period 1958–1978 is lower than for period 1994–2014 (Table 1 and Figure S1a). The earlier period depicts lower ISD for NINO3.4 SST index than later period till May afterward ISD for NINO3.4 SST is almost the same during July and September.

The climatological differences of rainfall between JIR P58-78 and P94-14 during May depict less precipitation over most of the Pacific region north of 10°N while more precipitation most of the equatorial Pacific region (Figure 2a). The climatological differences of JJ rainfall depict enhance precipitation over most of the tropical domain between 0° and 8°N while the reverse is true farther north around 15°N in the western Pacific (Figure 2b). The JIR P58-78 depicts less precipitation over the maritime continent, which extends westward into the equatorial Indian Ocean and southeastward into the South Pacific than JIR P94-14 (Figure 2b). It is interesting to note that the systematic JJ rainfall difference over Indian landmass is a part of the general pattern of precipitation difference in the Indo-Pacific region (Figures 2b and 2d). The precipitation difference between JIR P58-78 and P94-14 is associated with SST difference between earlier and later periods in the Indo-Pacific basin in the reforecasts. The warmer SST in the equatorial Pacific in the difference between JIR P58-78 and P94-14 extends from the eastern coastline to about 170°W (Figures 1b and 1c). Based on the observational and modeling results, many researchers (e.g., Kirtman & Shukla, 2000; Lau & Nath, 2000; Webster & Yang, 1992, and others) suggest that warmer SST in the equatorial Pacific generally corresponds to reduce Indian summer monsoon rainfall. It is found that the difference between JIR P58-78 and P94-14 depicts warm SST over the eastern equatorial Pacific during early summer that may lead to below normal rainfall over the Indian landmass (e.g., Kirtman & Shukla, 2000; Lau & Nath, 2000; Webster & Yang, 1992).
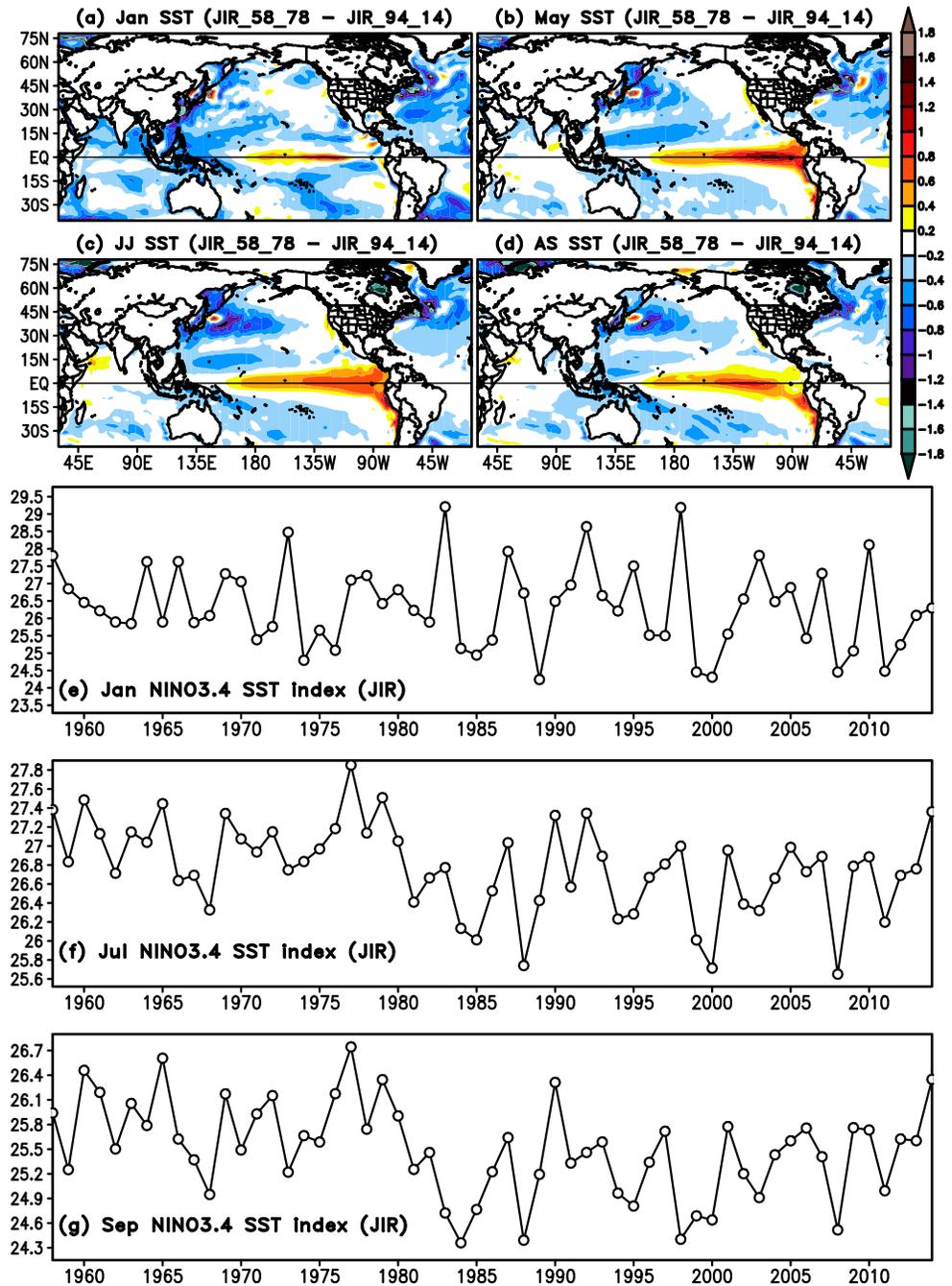
Figure 1. (a) Spatial distribution of the climatological difference of January (Jan) SST between JIR during mean of period 1958–1978 (P58-78) and period 1994_2014 (P94-14). (b) As in (a) but for May SST in JIR. (c) As in (a) but for mean of June to July (JJ) SST in JIR. (d) As in (a) but for mean of August to September (AS) SST in JIR. (e) Year-to-year variations of actual value of January NINO3.4 SST index in JIR for period 1958–2014. (f) As in (e) but for July NINO3.4 SST index. (g) As in (e) but for September NINO3.4 SST index.

Although the spatial distribution of climatological SST in both periods of JIR (Figures S2a–S2f) generally resembles the ERSSTv5 pattern (Figures S3a–S3f) but a systematic SST bias is found in both periods of reforecasts (Figures S4a–S4f). The JIR (P58-78; Figure S4a) depicts less cooling bias over the central Pacific in the first month of reforecasts in comparison to the later period JIR (P94-14; Figure S4d). The JIR (P58-78) depicts warm SST biases in the Pacific mainly between 45°N and 60°N and in the southern portion of the eastern

Table 1

The Interannual Standard Deviation (ISD) of Predicted Nino 3.4 SST Index in JIR for 1958–1978 (First Left Column) and for 1994–2014 (Second Left Column) During January to September

	JIR ISD (SST)		AprIR ISD (SST)		ERSSTv4 ISD (SST)	
	1958–1978	1994–2014	1958–1978	1994–2014	1958–1978	1994–2014
January	0.98	1.33			1.04	1.05
February	0.85	1.28			0.85	0.87
March	0.70	1.06			0.63	0.63
April	0.65	0.91	0.51	0.62	0.49	0.46
May	0.59	0.80	0.58	0.66	0.45	0.43
June	0.45	0.62	0.62	0.60	0.54	0.47
July	0.34	0.44	0.63	0.67	0.61	0.56
August	0.36	0.42	0.70	0.80	0.70	0.71
September	0.47	0.51	0.77	0.90	0.80	0.82

Note. The ISD of predicted Nino 3.4 SST index in AprIR for 1958–1978 (first middle column) and for 1994–2014 (second middle column) during April to September. The ISD of observed Nino 3.4 SST index in ERSSTv4 for 1958–1978 (second right column) and for 1994–2014 (second right column) during January to September.

Pacific, mainly between 20°S and 3°N during JJ and AS (Figures S4b and S4c), it may due to deficiencies in the simulation of clouds (e.g., Pan et al., 2011; Yoo et al., 2013). The magnitude of the warm bias is less in the JIR (P94-14; Figures S4e and S4f) over the southern portion of the eastern Pacific during JJ and AS in comparison to JIR (P58-78) but the magnitude of cold SST bias over the equatorial central Pacific is larger in the recent period (Figures S4e and S4f) in comparison to earlier period (Figures S4b and S4c). The JIR (P94-14) depicts severe dry bias over Indian landmass and excessive rainfall in the central Indian Ocean and in the northern Pacific Ocean during JJ and AS (Figures S4g and S4h), and a possible cause for the summer rainfall bias in long CFSv2 simulation is discussed in Shukla and Huang (2015).

The climatological difference in AprIR P58-78 and P94-14 does not depict any systematic shift of SST over the equatorial eastern Pacific during April, May, JJ, and AS (Figures S5a–S5d). The magnitude of ISD of predicted NINO3.4 SST index in AprIR for period 1958–1978 is almost equal to ISD for period 1958–1978 from June to September (Table 1 and Figures S5e–S5g). The difference of ERSSTv5 P58-78 and P94-14 does not depict warm SST over the equatorial eastern Pacific during summer but cold SST up to −0.6°C is found in the Indian Ocean, tropical Pacific, and the northern Atlantic Ocean during summer (Figures S6c and S6d). The magnitude of ISD of ERSSTv5 for 1958–1978 is almost equal to the ISD for 1994–2014 from January to September (Table 1).

The results reveal a systematic shift of predicted SST over the equatorial eastern Pacific in the climatological difference of SST between JIR P58-78 and P94-14, whereas AprIR and also ERSSTv5 do not depict a systematic shift of SST over the eastern Pacific. The same version of the coupled CFSv2 model is employed for generating the reforecasts for periods 1958–1978 and 1994–2014 in the January case. The instantaneous restart files for OICs are taken for the same source for the whole period. This may raise a question: What are possible causes for the systematic shift of predicted SST over the equatorial eastern Pacific in JIR before and after 1979? It may possible that the accuracy of subsurface potential temperatures and currents in the instantaneous restart files of the ECMWF ORAS4 (Balmaseda et al., 2013) on 1 January during 1994–2014 is much better than the 1 January during 1958–1978, which may be a possible cause for the systemic shift of SST and rainfall in the tropical region during summer in the JIR. In the next section, the impact of subsurface potential temperature and currents conditions in the seasonal reforecasts will be discussed.

4. Impact of Subsurface OICs on the Spatial and Temporal Variability of SST and Rainfall

First, I would like to discuss the climatological difference of mixed layer depth (MLD; Figure 3) and mean potential temperature from 5 to 195 m (MPT; Figure 4) between JIR P58-78 and P94-14. Ocean MLD is one of the most important variables in the air-sea interactions because MLD acts as an interface between the atmosphere and interior Ocean. It modulates heat exchange and energy between the ocean and atmosphere. MLD defines the region in the upper ocean where density or temperature is nearly vertically
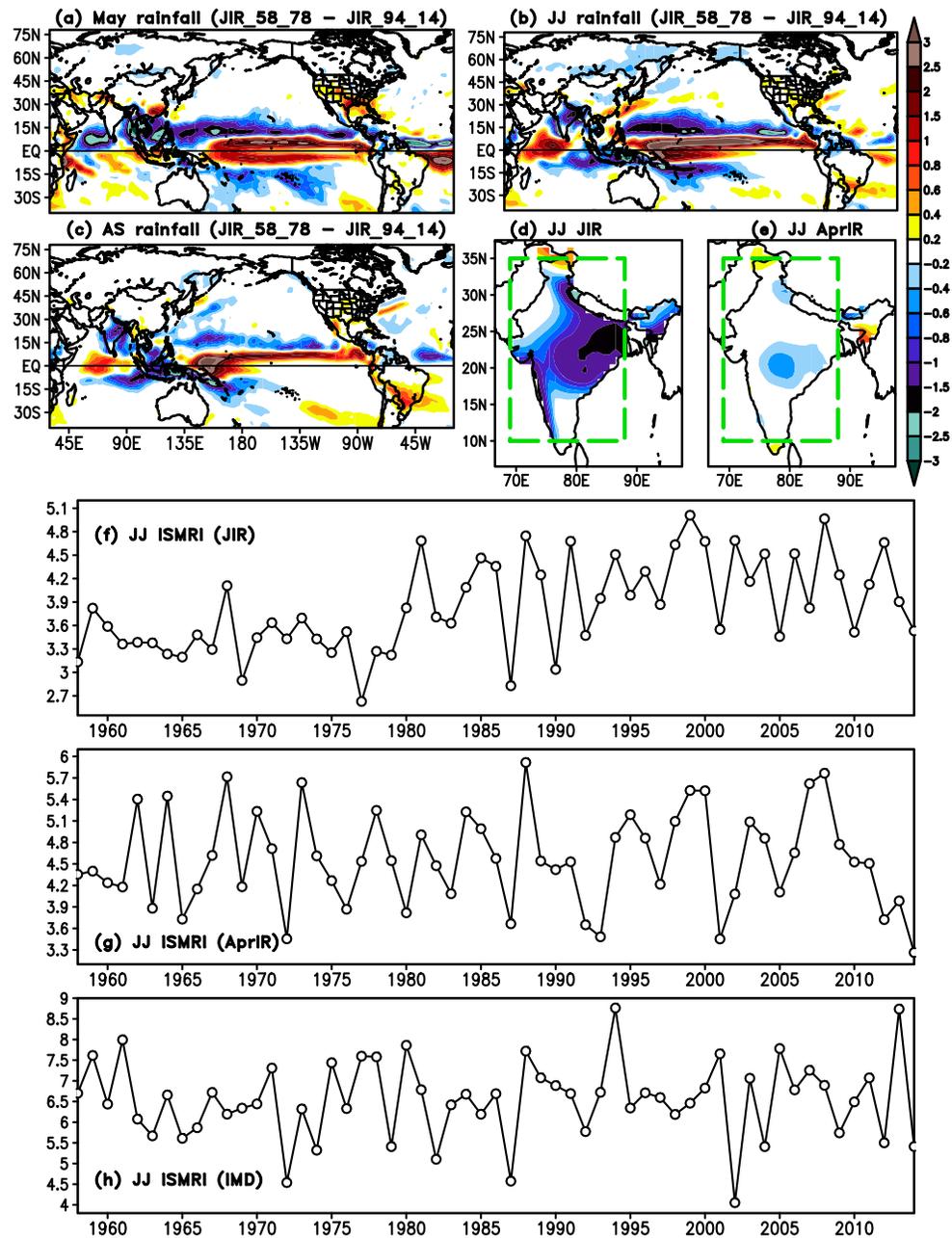
Figure 2. (a) Spatial distribution of the climatological difference of mean March to April (MA) rainfall between JIR during mean of P58-78 and P94-14. (b and c) As in (a) but for JJ and AS rainfall in JIR. (d) As in (a) but JJ rainfall in JIR over Indian landmass. (e) As in (a) but JJ rainfall in AprIR over Indian landmass. (f) Year-to-year variations of JJ actual value of rainfall index over Indian landmass (green box in Figure 2d: 10–35°N, 69–88°E) in JIR for period 1958–2014. (g) As in (f) but for JJ rainfall index over Indian landmass in AprIR. (h) As in (f) but for JJ rainfall index over Indian landmass in IMD rainfall.

uniform. Consistent with previous studies (e.g., Alexander et al., 2000; Huang et al., 2012), the JIR P94-14 depicts deep (shallow) MLD in the western central (eastern) tropical Pacific during January to February (Figures S7a and S7b). During March and April (Figures S7c and S7d), the magnitude of MLD decreases over the western-central in comparison to January (Figure S7a). As lead months increase (June to September; Figures S7f–S7i), the magnitude of MLD increases gradually over the western central tropical Pacific. The climatological difference of MLD between JIR P58-78 and P94-14 in January (Figure 3a)
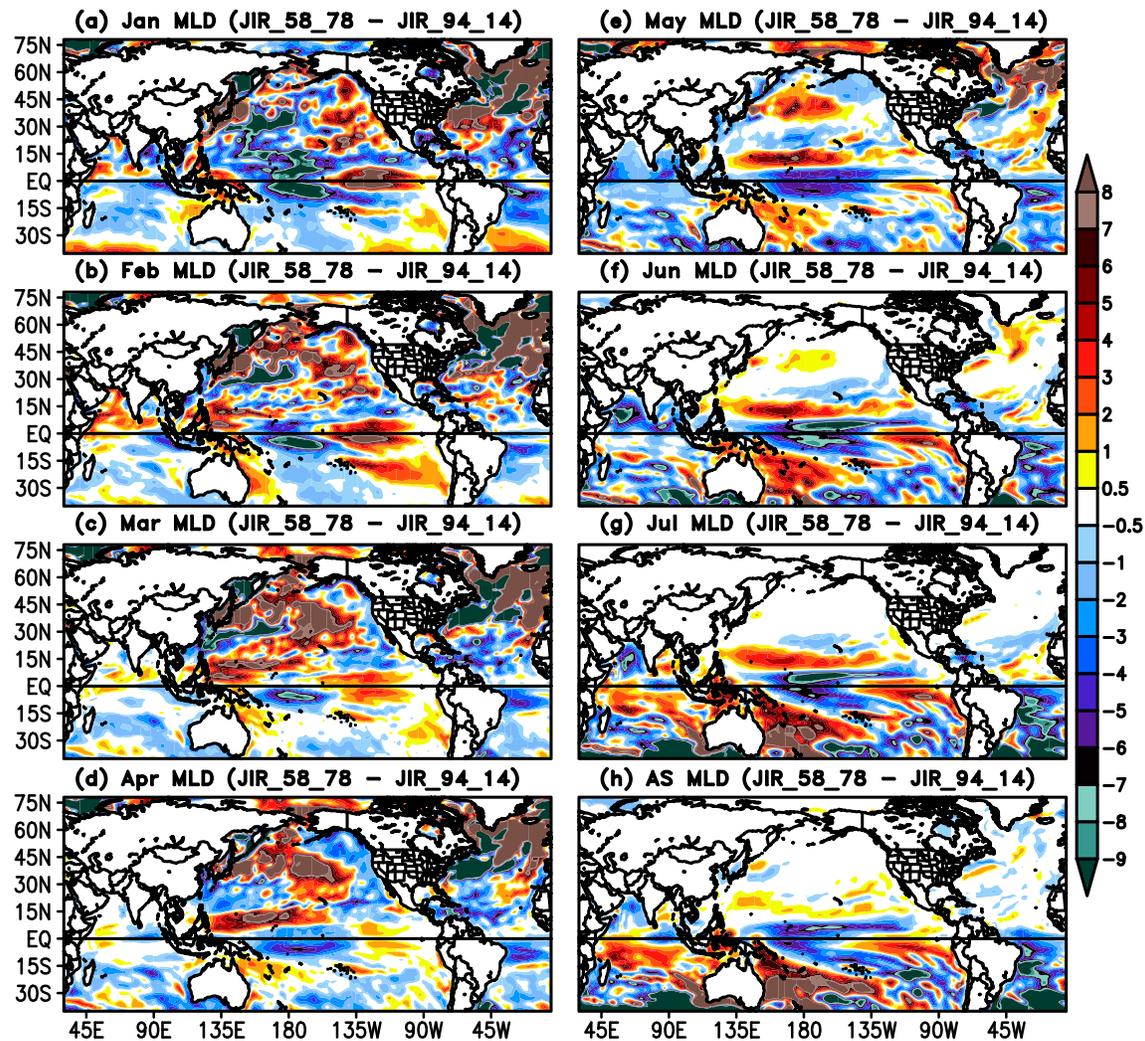
Figure 3. (a) Spatial distribution of the climatological difference of January mixed layer depth (MLD) between JIR during mean of P58-78 and P94-14. (b–h) As in (a) but for February (b), March (c), April (d), May (e), June (f), July (g), and AS (h) MLD in JIR.

depicts shallower-than-average (deeper-than-average) values of MLD up to 9 m in the equatorial western (eastern) Pacific but the magnitude of MLD decreases over there during February and March (Figures 3b and 3c). As lead months increase (from April to September; Figures 3d–3h), the model depicts the tendency of shallower-than-average MLD up to 8 m over the western central tropical Pacific, mainly between (5°S to 5°N, 150–210°E) and deeper-than-average MLD over the eastern tropical Pacific during summer (Figures 3f–3h).

The climatological difference of MPT between JIR P58-78 and P94-14 depicts warm temperature up to 1.8°C over the central tropical Pacific mainly between 200°E and 250°E (Figure 4a), but the magnitude of warm temperature slightly decreases in February (Figure 4b) over there. From March to April (Figures 4c and 4d), the center of warm MPT extending farther to the eastern Pacific than its location in January (Figure 4a). From May to September, the difference in JIR P58-78 and P94-14 depicts warm MPT up to 1°C over the equatorial eastern Pacific whereas cold MPT over the western Pacific (Figures 4e–4h). The magnitude of warm MPT over the equatorial central Pacific in January (Figure 4a) is much larger than the magnitude of warm SST over there in January (Figure 1a). The magnitude of warm MPT and SST is almost similar over the equatorial eastern Pacific from June to September.

On the other hand, the magnitude of the climatological difference of MLD between AprIR P58-78 and P94-14 is small over the equatorial western Pacific in April whereas it is up to 3 meters in the equatorial
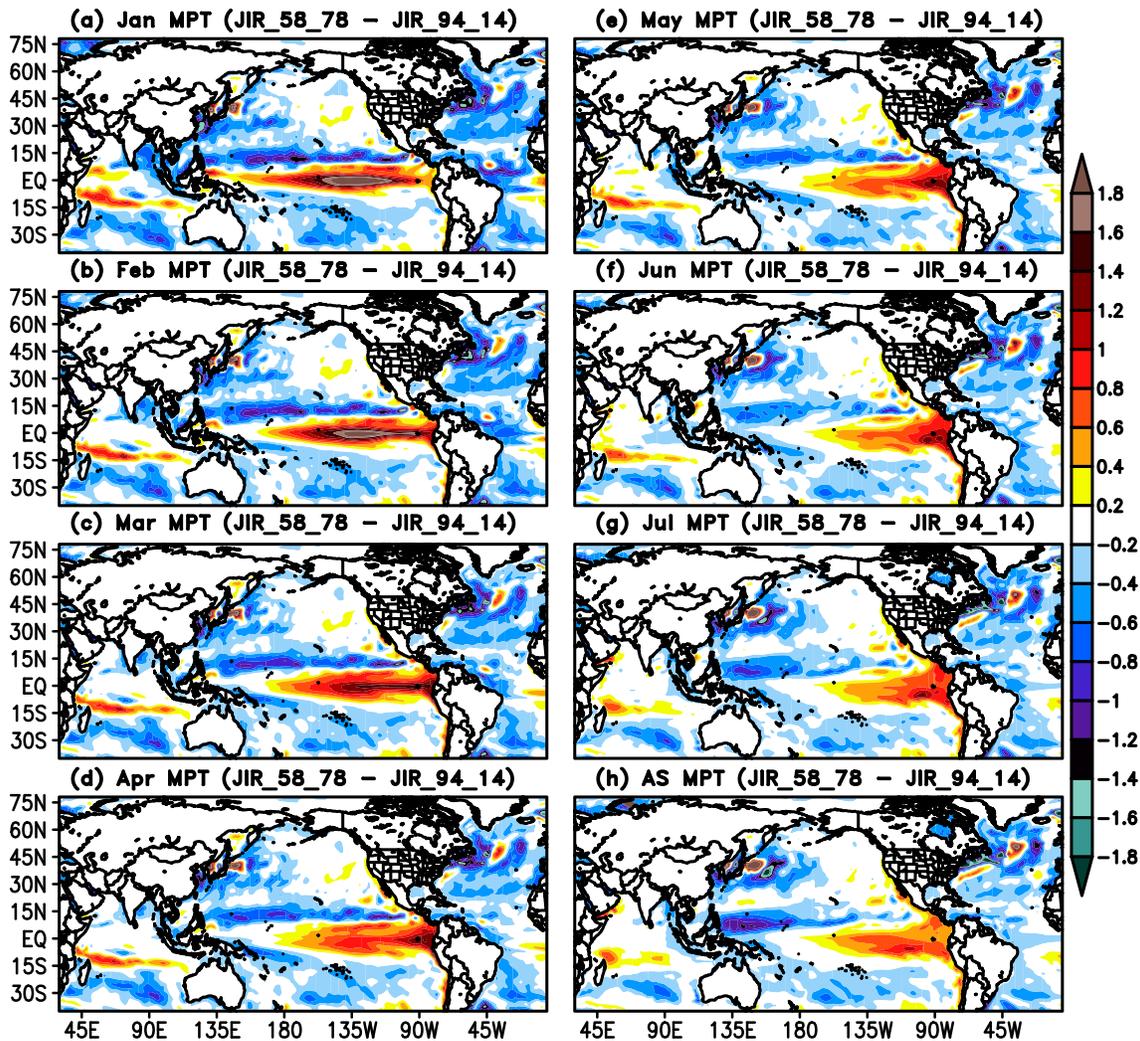
Figure 4. (a) Spatial distribution of the climatological difference mean potential temperature from 5 to 195 m (MPT) in January between JIR during mean of P58-78 and P94-14. (b–h) As in (a) but for February (b), March (c), April (d), May (e), June (f), July (g), and AS (h) MPT.

eastern Pacific (Figure 5a). As lead months increase (March to September; Figures 5b–5d) the climatological difference of MLD over the equatorial western and eastern Pacific is small. The climatological difference of MPT between AprIR P58-78 and P94-14 depicts a warm temperature up to 1°C over the equatorial eastern Pacific (Figure 5e). As lead months increase, the magnitude of warm MPT decreases gradually from May to September (Figures 5f–5h). It is necessary to mention that the climatological difference between AprIR P58-78 and P94-14 depicts warm MPT from April to September over the equatorial eastern Pacific (Figures 5e–5h), but the magnitude of warm SST over there is negligible (Figures S5a–S5d).

Figures 6a–6e show the vertical sections (latitude averaged from 1°S to 1°N) of climatological potential temperature (PT) during January, February, May, June, and August in the JIR P94-14, respectively. The JIR P94-14 generally reproduces the depth and strength of the thermocline in January and February as reported in previous studies (Johnson et al., 2002; Shaji et al., 2005). Qualitatively, JIR P94-14 depicts the magnitude and vertical structure of PT in January and August over the equatorial Pacific Ocean as observation (WOA 09; Locarnini et al., 2010; Figures S8a and S9a) and multiple reanalyses do (Figures S8b–S8e and S9b–S9e) respectively. The dotted black line indicates 20°C isotherm (Z20) which is a measure of thermocline depth in the tropical Pacific. During January and February, the SEC is generally confined above 35 m in the eastern Pacific, but gradually thickens toward the western Pacific about 110 m between 150°E and 180°E in JIR P94-14 (Figures 6f–6g). The equatorial undercurrent (EUC), a strong eastward subsurface jet, is deep in
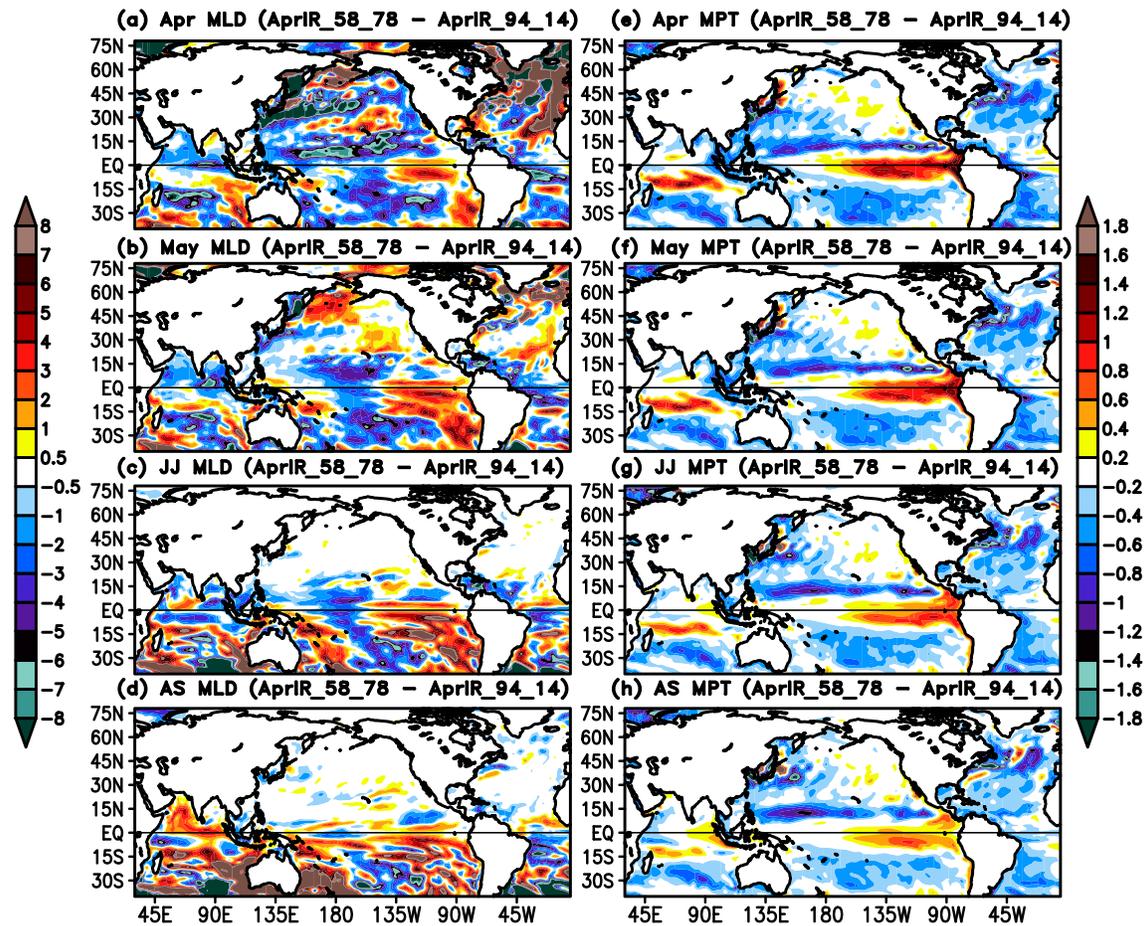
Figure 5. Spatial distribution of the climatological difference of MLD between AprIR during mean of P58-78 and P94-14 in April (a), May (b), JJ (c), and AS (d). The scale for the magnitude for MLD in "m" is shown at left of these panels. (e–h) As in (a) and (b) but for MPT between AprIR during mean of P58-78 and P94-14. The scale for the magnitude for MPT in "°C" is shown at right of these panels.

the western Pacific and slopes upward in the eastern Pacific during January and February in the JIR P94-14 (Figures 6f–6g). A similar feature of the EUC has been observed in the observational and modeling studies (Johnson et al., 2002; Large & Danabasoglu, 2006; McPhaden, 2004; Shaji et al., 2005; Wittenberg et al., 2006; Yeager et al., 2006). Qualitatively, JIR P94-14 depicts the magnitude and vertical structure of the EUC and SEC in January and August over the equatorial Pacific Ocean as multiple reanalyses do respectively (Figures S8k–S8n and S9k–S9n). In January, the maximum magnitude of EUC is 60 cm/s at 145°W at depth of about 125 m. The magnitude of EUC is around 80 cm/s between 150°W and 120°W at depth of 100 to 115 m in May. From April to June, warm water from the surface of the western Pacific penetrates downward in the eastward direction within 185 m in JIR P94-14 (Figures 6c–6d, S10d and S10e) and therefore the EUC transports warm water in the eastern Pacific region during this period, which also enhances the magnitude of SST over the equatorial eastern Pacific. Consistent with it, the isotherm (Z20) tends to be deeper in May and June (black line; Figures 6c and 6d) in the eastern Pacific in comparison to its locations in January (dotted black line) in the JIR P94-14. Due to the combined effect of the eastern equatorial upwelling along the coast of Peru and SEC, the eastern equatorial Pacific displays cold-water farther toward the equatorial western Pacific from July to August (Figures 6e, 6j, and S10g–S10i).

The magnitude of salinity in January of JIR P94-14 is between 35.3 and 35.4 psu at depth from 170 to 125 m over the equatorial western Pacific whereas its magnitude is between 33.4 and 34.7 psu at depth from 35 to 5 m over the equatorial western and central Pacific (Figure 6k). Qualitatively, JIR P94-14 reproduces the magnitude and vertical structure of salinity in January and August over the equatorial Pacific as observation (WOA 09; Antonov et al., 2010; Figures S6f and S7f) and multiple reanalyses do (Figures S8f–S8j and S9f–S9j)
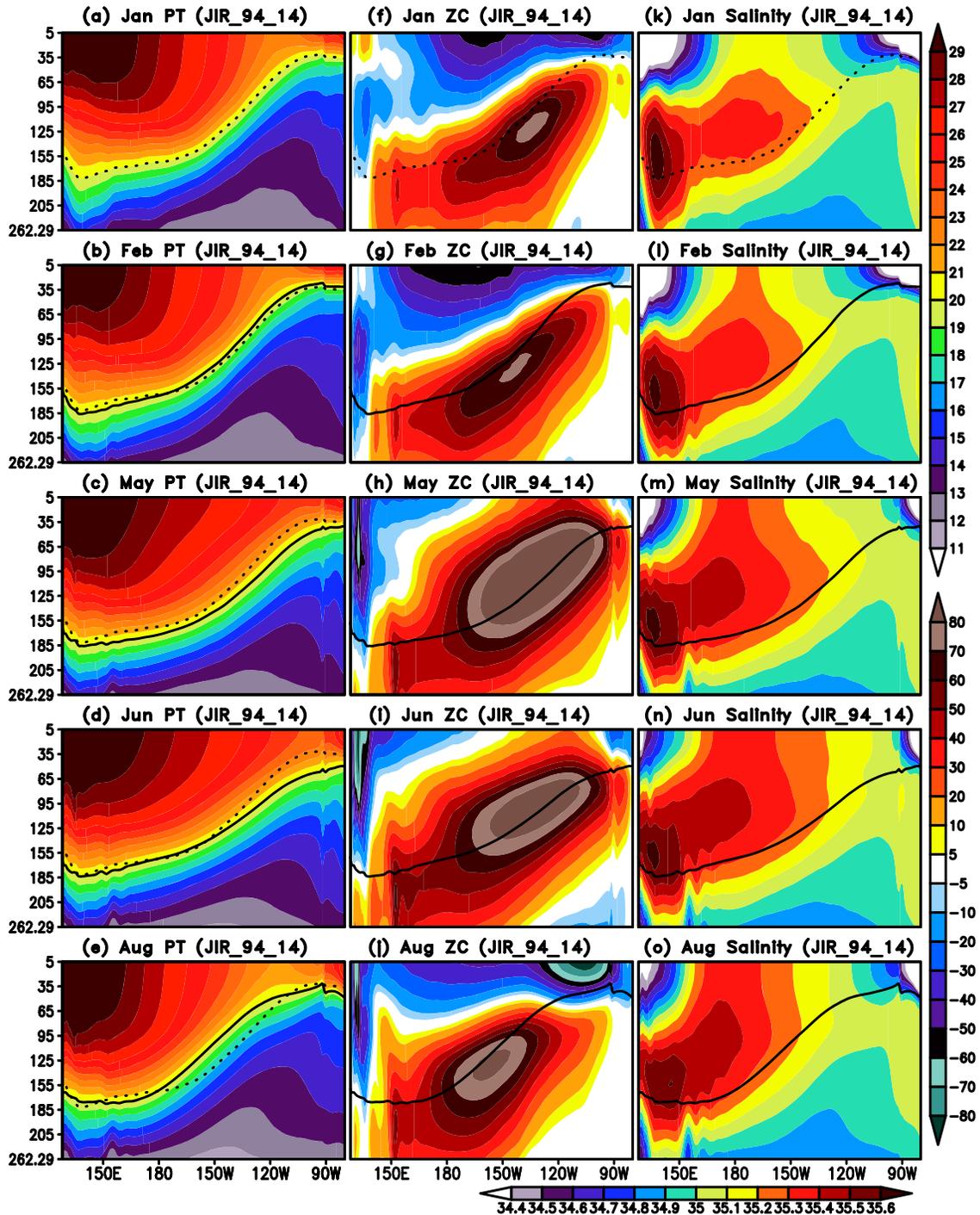
Figure 6. Longitude-depth section (latitude averaged from 1°S to 1°N) of climatological mean of PT in JIR during mean of P94-14 for (a) January, (b) February, (c) May, (d) June, and (e) August. The scale for the magnitude of PT in "°C" is shown at right of these panels (upper one). The dotted black line indicates 20°C isotherm (Z20) in January of JIR P58-78. The black line indicates Z20 for February to August in the JIR P58-78. (f–j) As in (a) and (b) but for zonal current (ZC) in JIR during mean of P94-14. The scale for the magnitude of ZC in "cm/s" is shown at right of these panels (below one). (k–o) As in (a) and (b) but for salinity in JIR during mean of P94-14. The scale for the magnitude of salinity in "psu" is shown below these panels.
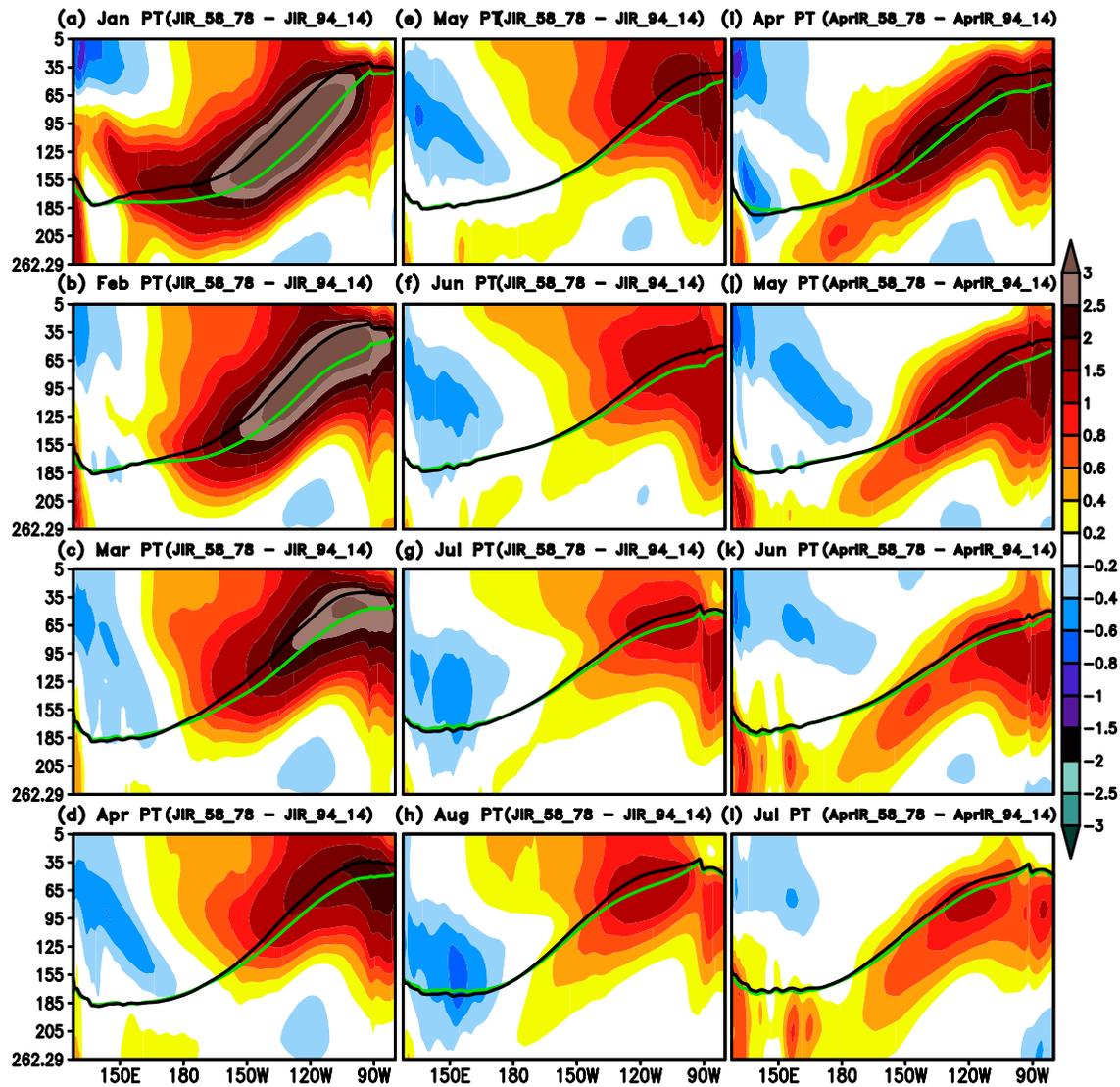
Figure 7. (a) Longitude-depth section (latitude averaged from 1°S to 1°N) of climatological difference of Jan PT between JIR during mean of P58-78 and P94-14. (b–h) As in (a) but for February (b), March (c), April (d), May (e), June (f), July (g), and August (h) PT in JIR. The green line (black line) indicates 20°C isotherm (Z20) in the period P58-78 (P94-14) in both JIR and AprIR. (i) Longitude-depth section (latitude averaged from 1°S to 1°N) of climatological difference of Apr PT between AprIR during mean of P58-78 and P94-14. (j–l) As in (i) but for May (j), June (k), and July (l) PT in AprIR.

respectively. As the lead months increase, the magnitude of salinity increases over the equatorial Pacific (Figures 6l–6o).

Figures 7 and 8 depict the vertical sections (latitude averaged from 1°S to 1°N) of climatological differences of potential temperature and zonal current (ZC) between the mean of periods P58-78 and P94-14 in both JIR and AprIR. The green line (black line) indicates 20°C isotherm (Z20) for the period P58-78 (P94-14) in both JIR and AprIR in Figures 7 and 8. The vertical section of PT is warmer up to 3°C over the equatorial central and eastern Pacific mainly between 150°W and 100°W at depth from 155 to 70 m in January (Figures 7a and S11) therefore Z20 of JIR P58-78 (green line in Figure 7a) in January tends to be deeper in the equatorial eastern Pacific in comparison to its locations in JIR P94-14 (black line in Figure 7a). The difference of zonal currents between JIR P58-78 and P94-14 in January depicts enhance magnitude of the EUC in the eastern Pacific at depth from 125 to 35 m up to 24 cm/s, and also weaker magnitude of the SEC in the western and eastern Pacific, which confined above 35 m (Figure 8a). Since thermocline is deeper and zonal currents is enhance in JIR P58-78 in comparison to JIR P94-14 in the equatorial eastern Pacific in January, water
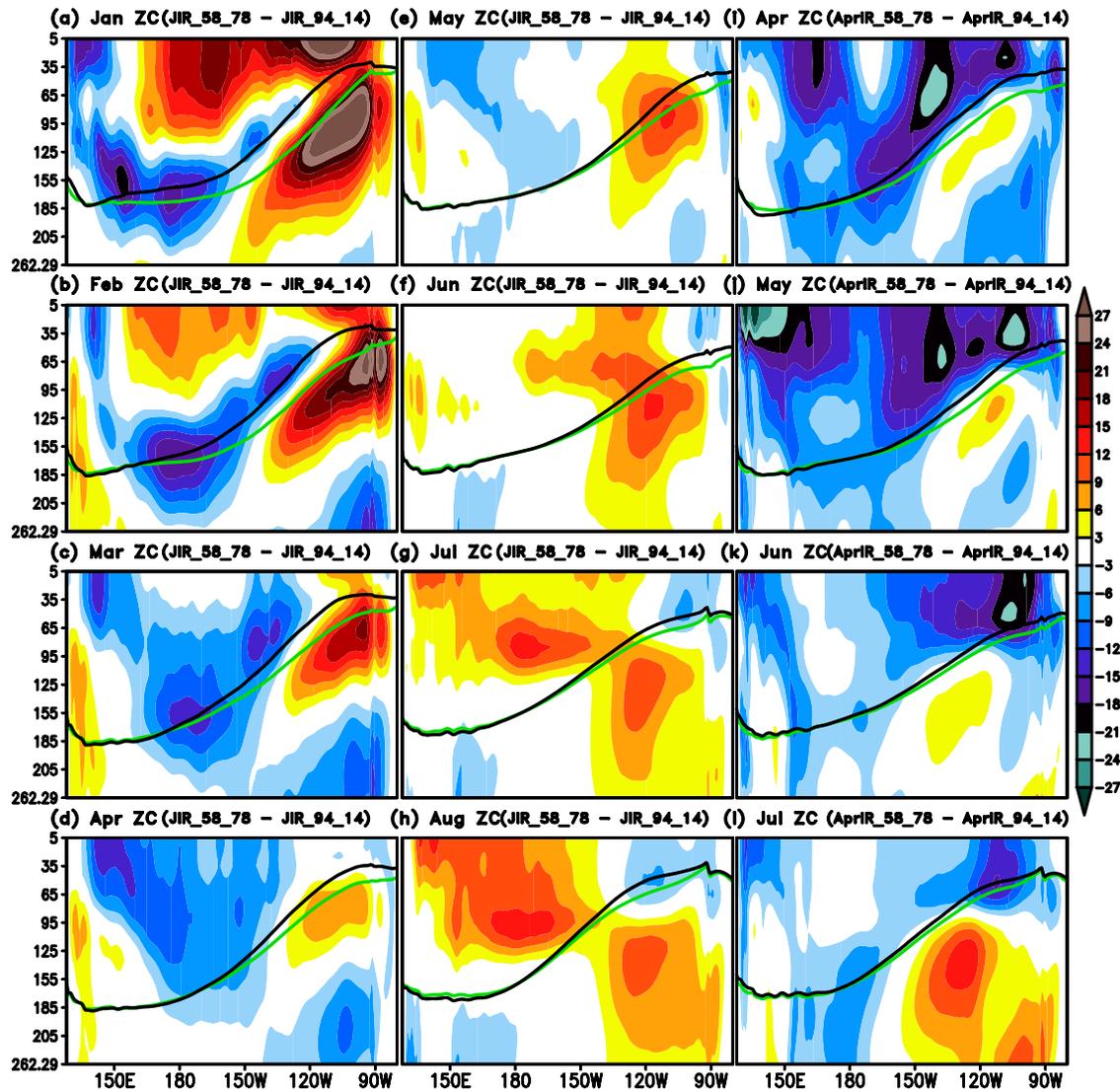
Figure 8. (a) Longitude-depth section (latitude averaged from 1°S to 1°N) of climatological difference of Jan zonal current between JIR during mean of P58-78 and P94-14. (b–h) As in (a) but for February (b), March (c), April (d), May (e), June (f), July (g), and August (h) zonal current in JIR. The green line (black line) indicates 20°C isotherm (Z20) in the period P58-78 (P94-14) in both JIR and AprIR. (i) Longitude-depth section (latitude averaged from 1°S to 1°N) of climatological difference of Apr zonal current between AprIR during mean of P58-78 and P94-14. (j–l) As in (i) but for May (j), June (k), and July (l).

upwelled to the surface through the EUC was usually warm. From February and March (Figures 7b and 7c), the center of warm PT gradually moves upward in the eastern Pacific than its location in January. The center of warm PT (up to 2.5°C) is generally confined between 80 and 35 m in March, resulting in the development of warm SST in the eastern Pacific. The difference of zonal currents between JIR P58-78 and P94-14 during February and March (Figures 8b and 8c) depicts the larger magnitude of the EUC in JIR P58-78 in the eastern Pacific but smaller than in January (Figure 8a). As the center of warm PT moves gradually upward in the eastern Pacific, the difference in locations of isotherm (Z20) between JIR P58-78 and P94-14 in March (Figure 7c) decreases in the central eastern Pacific in comparison to its difference in January (Figure 7a). A warm PT up to 1°C persists between 65 and 5 m in the eastern Pacific from April to August (Figures 7d–7h), resulting in warm SST anomalies over the equatorial eastern Pacific during summer. The difference in locations of isotherm (Z20) between JIR P58-78 (green line in Figures 7g and 7h) and JIR P94-14 (black line in Figures 7g and 7h) from July to August is negligible except 135–110°W. From July to August, the magnitude of SEC is weaker over the western Pacific in JIR P58-78 in comparison to JIR P94-14.
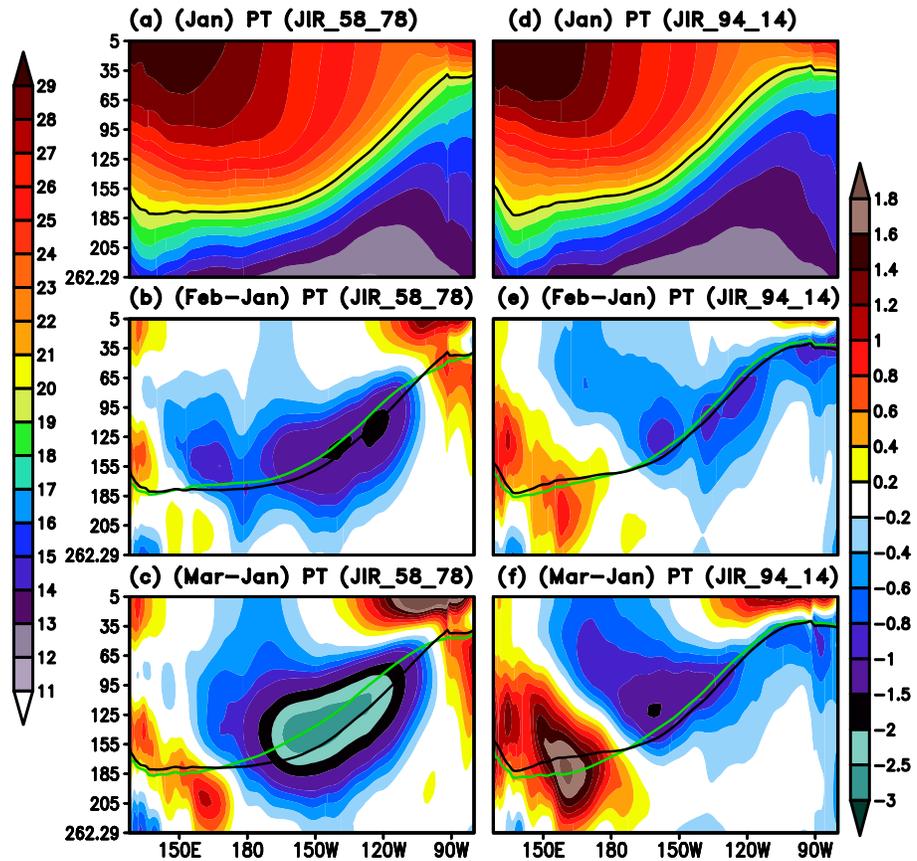
Figure 9. (a) Longitude-depth section (latitude averaged from 1°S to 1°N) of climatological mean PT in JIR during mean of P58-78 in January. The scale for magnitude of PT in "°C" is shown at left of this panel. The black line indicates 20°C isotherm (Z20) in January in JIR P58-78. The climatological change of PT with respect to January for (b) February and (c) March in JIR. The scale for change in PT in "°C" is shown at right of this panel. The green line indicates Z20 in February and March in JIR P58-78. (d–f) As in (a)–(c) but for JIR during mean of P94-14 PT.

The difference of PT between AprIR P58-78 and P94-14 depicts warm temperature up to 1.5°C in the equatorial eastern Pacific mainly between 150°W and 90°W at depth from 135 to 35 m in April (Figure 7i). The AprIR P58-78 isotherm (Z20; green line) in April is slightly deeper in the eastern Pacific in comparison to its locations in AprIR P94-14 (black line). From May to July, the magnitude of warm PT gradually decreases in the eastern Pacific (Figures 7j–7l) and there is no tendency of gradually upward movement of warm water in the eastern Pacific than its location in January (Figure 7i), resulting in negligible differences in magnitude of SST between AprIR P58-78 and P94-14 over the eastern Pacific during summer (Figures S5a–S5d). The difference of zonal current between AprIR P58-78 and P94-14 does not depict large value of the EUC from April to July (Figures 8i–8l). The difference of salinity between JIR (AprIR) P58-78 and P94-14 depicts low value at depth from 185 to 125 m over the equatorial central Pacific in the first month of reforecasts (Figures S12a and S12i). As lead months increase, the magnitude of salinity is negligible in both JIR (Figures S12b–S12h) and AprIR (Figures S12j–S12l).

Due to the warmer-than-average value of PT in January over the equatorial central and eastern Pacific in JIR P58-78, the climatological shift in February PT with respect to January depicts colder PT up to 1°C in the central Pacific from 185 to 95 m and warmer PT up to 0.8°C from 35 to 5 m (Figure 9b). The Z20 of January (black line in Figure 9b) is slightly deeper than Z20 of February (green line in Figure 9b) in the central Pacific; it may imply that the JIR P58-78 losses heat in the central Pacific due to the upwelling of warm water to the surface in February. The climatological shift of PT in March with respect to January PT in JIR P58-78 depicts severe cold PT up to 3°C in the central Pacific from 155 to 95 m and warmer PT up to 1.8°C from 35 to 5 m in March (Figure 9c), and also the Z20 of January (black line in Figure 9c) is deeper than Z20
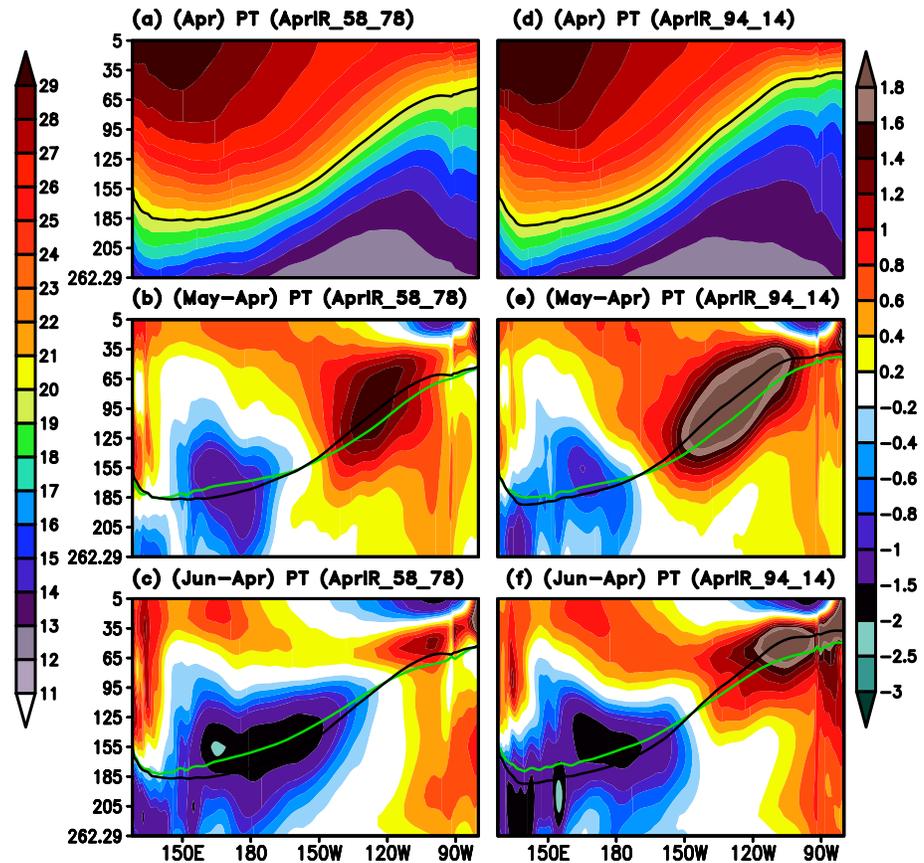
Figure 10. (a) Longitude-depth section (latitude averaged from 1°S to 1°N) of climatological mean PT in AprIR during mean of P58-78 in April. The scale for magnitude of PT in "°C" is shown at left of this panel. The black line indicates 20°C isotherm (Z20) in January in JIR P58-78. The climatological change of PT with respect to April for (b) May and (c) June in AprIR. The scale for change in PT in "°C" is shown at right of this panel. The green line indicates Z20 in February and March in JIR P58-78. (d–f) As in (a)–(c) but for AprIR during mean of P94-14 PT.

of March (green line in Figure 9c) in the central Pacific. On the other hand, the climatological shift of PT in February and March with respect to January PT in JIR P94-14 (Figures 9e and 9f) does not depict large cold PT in the central Pacific from 155 to 95 m in comparison to JIR P58-78 (Figures 9c and 9d), and also the Z20 of January (black line in Figure 9e) is almost same locations in the central Pacific as in Z20 of February (green line in Figure 9e) and March (green line in Figure 9f) in JIR P94-14. The warm water from the surface of the equatorial western Pacific penetrates downward in the eastward direction within 185 m during February and March in JIR P94-14 (Figures 9e and 9f), resulting in Z20 of March (green line in Figure 9f) over the western Pacific is deeper than Z20 of January around 185 m. The magnitude of warm PT from 155 to 205 m over the western Pacific in March is much less in JIR P58-78 (Figure 9c) in comparison to JIR P94-14 (Figure 9f) therefore most of the warm water transports through the EUC during February and March in JIR P58-78 is mainly due to warmer-than-average values of PT during January and February in the equatorial central and eastern Pacific.

The climatological shift of PT in May with respect to PT of April in AprIR P58-78 (Figure 10b) and AprIR P94-14 (Figure 10e) depict the tendency of warm PT in the eastern Pacific from 155 to 65 m. The Z20 of May in both AprIR P58-78 and AprIR P94-14 (green line in Figures 10b and 10e) is deeper than Z20 of April (black line in Figures 10b and 10e); it may imply that warm water from surface of the equatorial western Pacific penetrates downward in eastward direction within 125 m in May. It is also found that Z20 of June (green line in Figure 10f) in AprIR P94-14 is deeper in the eastern Pacific than Z20 of April (black line in Figure 10e). The magnitude of climatological shift in May PT with respect to April in AprIR P58-78 (Figure 10b) is less in comparison to AprIR P94-14 (Figure 10e) because the magnitude of PT during April and May in the AprIR P58-78 is larger up to 1°C in comparison to AprIR P94-14 (Figures 7i and 7j).
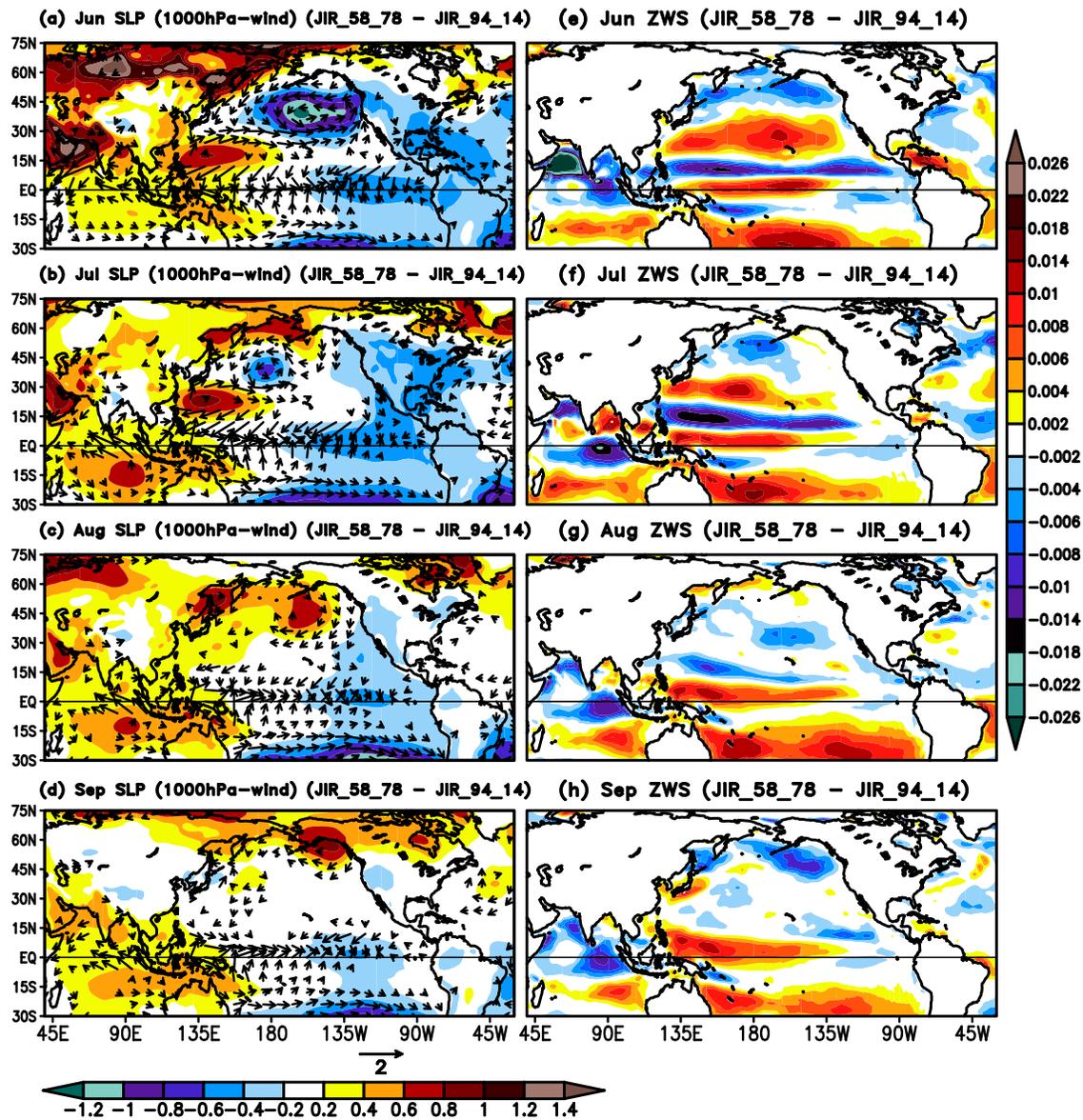
Figure 11. Spatial distribution of the climatological difference of January SLP (in shading) and 1,000-hPa winds (in vector) between JIR during mean of P58-78 and P94-14 (a) June, (b) July, (c) August, and (d) August. The scale for magnitude of SLP is shown at right of these panels (upper one). (e and f) As in (a) and (b) but for zonal wind stress (ZWS; N/m^2). The scale for magnitude of ZWS is shown at right of these panels (lower one).

The climatological differences between JIR P58-78 and P94-14 depict slightly strong vertical current up to 0.5 m/day in January over the equatorial tropical Pacific from 65 to 5 m in the earlier period than later period (Figure S13a), where climatological mean value of vertical currents in the JIR (P94-14) is up to 1.2 m/day (Figure S14a). The vertical current is also slightly stronger in the JIR P58-78 than JIR P94-14 where Z20 of JIR P58-78 (green line) is deeper than the JIR P94-14 (black line) in January (Figure S13a). The stronger vertical current in the JIR (P58-78) may contribute to the upwelling warm water to the surface. As lead months increase, the magnitude of vertical current decreases gradually from February to March (Figures S13b–S13e). The climatological difference of vertical current between AprIR P58-78 and P94-14 does not depict a large difference in April over the equatorial Pacific Ocean (Figure S13i).

Quantitevaly, the JIR P94-14 (Figures S15d–S15f) depicts a reasonably vertical section (latitude averaged from 1°S to 1°N) of meridional current (MC) as CFSR do in January, March, and April in the Pacific Ocean (Figures S15a–S15c). The climatological difference of meridional current between JIR P58-78 and

P94-14 does not depict a large difference in January (Figure S16a) over the equatorial Pacific but as lead months increase, meridional current in the earlier period is slightly stronger in the equatorial western Pacific from March to April between 65 and 5 m than the later period (Figures S16c and S16d) that may indicate slightly strong heat transport toward southward in the western Pacific Ocean.

Consistent with warmer SST over the equatorial eastern Pacific (Figures 1b–1d), the difference between JIR P58-78 and P94-14 depicts below normal surface pressure over the equatorial eastern Pacific and above normal pressure over the western Pacific and Indian Ocean from June to September (Figures 11a–11d; shaded) and trade winds flow from east to west is weaken over the equatorial western-central Pacific from June and September (Figures 11a–11d; vector). The climatological differences of zonal wind stress (ZWS) in the mean of periods JIR P58-78 and P94-14 depicts the positive magnitude of ZWS over the equatorial western central Pacific from June to September (Figures 11e–11h). Below (above) normal surface pressure over the eastern Pacific (western Pacific and Indian Ocean) and weakening of trade winds consist of below normal rainfall over the maritime continent and Indian continent and above normal rainfall over the equatorial central Pacific during summer.

5. Summary and Discussion

This study investigates the potential impact of the subsurface potential temperature and current conditions on the spatial and temporal variability of SST and rainfall over the tropical region in 1958–2014 seasonal reforecasts, which is initialized in January and April. The OICs were taken from instantaneous restart files of ORAS4 for the whole period, but the quality of OICs should be different before and after 1979; therefore, the two time periods of 21-years in JIR and AprIR are defined, earlier period (1958–78) and later period (1994–2014).

The difference between JIR P58-78 and P94-14 depicts warm SST over the equatorial eastern Pacific in January but its magnitude became larger over there and expanding farther to the eastern Pacific during May and JJ. The earlier period depicts lower interannual variability for NINO3.4 SST index than later period till May afterward ISD for NINO3.4 SST is almost same in both periods during July and September. The climatological difference between JIR P58-78 and P94-14 depicts enhance precipitation over most of the tropical domain between 0° and 8°N and less over the maritime continent, which extends westward into the equatorial Indian Ocean and southeastward into the South Pacific. On the other hand, the climatological difference in AprIR P58-78 and P94-14 does not depict any systematic shift of SST over the equatorial eastern Pacific during summer.

The difference between JIR P58-78 and P94-14 depicts warm MPT up to 1.8°C over the equatorial central Pacific in January, but its center extending farther to the eastern Pacific during March and April therefore warm MPT up to 1°C persists over the equatorial eastern Pacific from May to September. The difference between JIR P58-78 and P94-14 depicts shallower-than-average (deeper-than-average) MLD in January over the equatorial western (eastern) Pacific but its magnitude decreases from February and March. The climatological difference between JIR P58-78 and P94-14 depicts warm SST over the equatorial eastern Pacific during summer, which is consist with shallower-than-average MLD over the western Pacific and deeper-than-average MLD over the eastern tropical Pacific during summer. On the other hand, the difference between AprIR P58-78 and P94-14 depicts warm MPT up to 1°C over the equatorial eastern Pacific but gradually decreases as lead months increase therefore the difference in MLD over the equatorial western and eastern Pacific is small.

The vertical sections of difference between JIR P58-78 and P94-14 during January depict warmer potential temperature up to 3°C in the equatorial central eastern Pacific and the enhanced the magnitude of the EUC in the eastern Pacific at depth from 125 to 35 m, and stronger vertical current in the earlier period than the later period over the equatorial tropical Pacific from 65 to 5 m, therefore, water upwelled to the surface through the EUC was usually warm. As lead month increases, the center of warm potential temperature gradually moves upward in the eastern Pacific and confined between 80 and 35 m in March, resulting in development of warm SST in the eastern Pacific. From April to August a warmer potential temperature up to 1°C persists between 65 and 5 m in the eastern Pacific, resulting in large difference in SST to 1°C in the eastern Pacific from May to July. On the other hand, the difference between AprIR P58-78 and P94-14 depicts a warm temperature up to 1.5°C in the eastern Pacific at depth from 135 to 35 m in April. The zonal
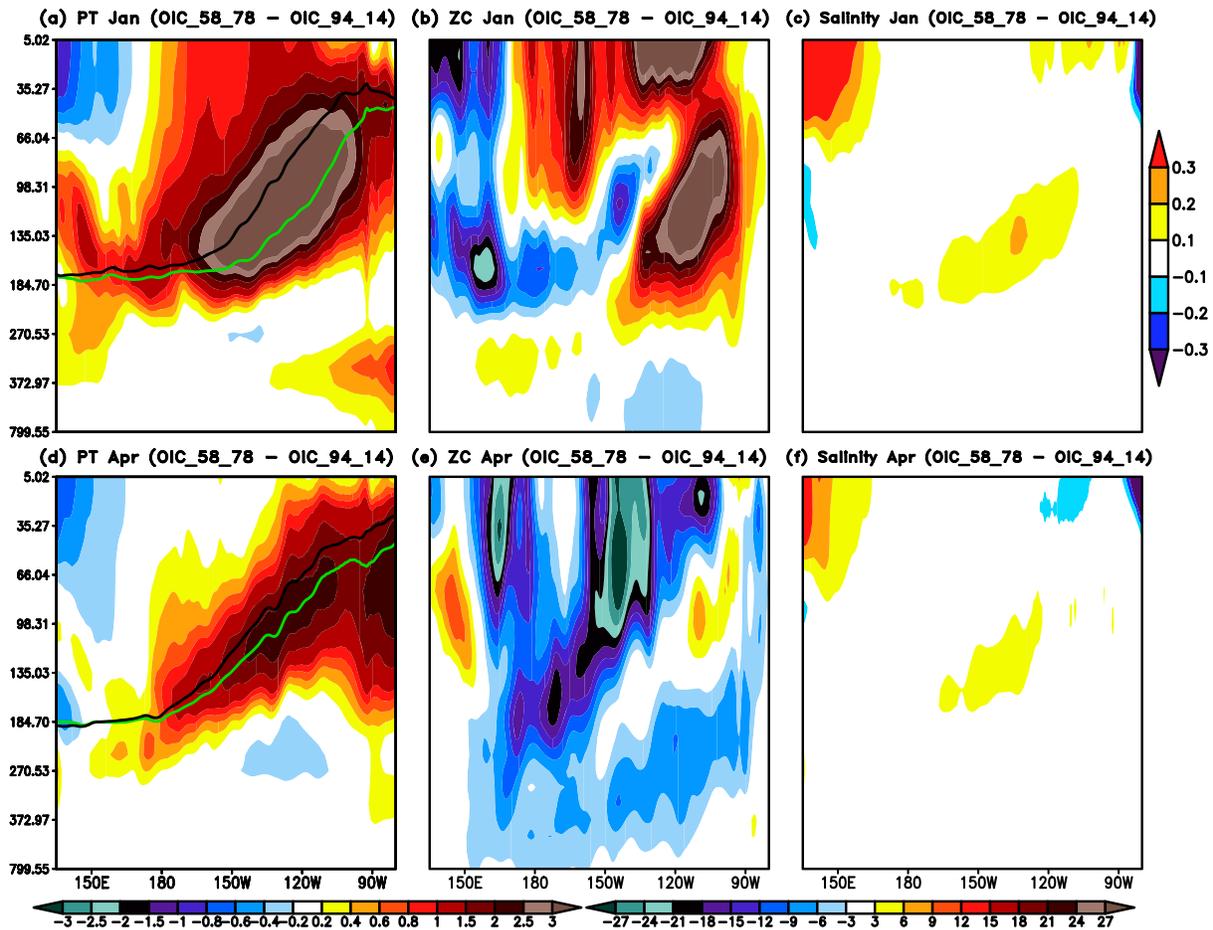
Figure 12. Longitude-depth section (latitude averaged from 1°S to 1°N) of climatological difference of OICs (ECMWF ORAS4) in January between mean of P58-78 and P94-14 for (a) PT, (b) ZC, and (c) salinity. The scale for the magnitude of PT in "°C" is shown below this panel. The scale for the magnitude of ZC in "cm/s" is shown below this panel. The scale for the magnitude of salinity in "psu" is shown at right of this panel. The green line (black line) indicates 20°C isotherm (Z20) in the period P58-78 (P94-14) in both JIR and AprIR. (d–f) As in the (a)–(c) but for the OICs (ECMWF ORAS4) in April.

current and vertical current are not stronger in the AprIR P58-78 than AprIR P94-14 in April over the equatorial tropical Pacific. As lead months increase, the magnitude of warm PT gradually decreases over there, resulting in a negligible difference in magnitude of SST over the eastern Pacific.

Due to the warmer-than-average potential temperature in January of JIR P58-78 over the equatorial central and eastern Pacific at depth from 155 to 70 m, resulting in warm water upwelled to the surface through the EUC in February, therefore, the climatological shift in February with respect to January depicts colder temperature up to 1°C in the central Pacific from 185 to 95 m and warmer temperature up to 0.8°C from 35 to 5 m. The Z20 of January is slightly deeper than Z20 of February in JIR P58-78; it may imply that the JIR P58-78 loses heat due to the upwelling of warm water to the surface in the central Pacific from 175 to 95 m. On the other hand, the climatological shift of temperature in February and March with respect to January in JIR P94-14 does not depict a large cold temperature in the central Pacific from 155 to 95 m, and the Z20 of January is almost the same locations in the central Pacific as in Z20 of February and March. The warm water from the surface of the equatorial western Pacific penetrates downward in the eastward direction within 185 m during February and March in JIR P94-14, resulting in Z20 of March over the western Pacific is deeper than Z20 of January around 185 m. The magnitude of warm temperature from 155 to 205 m over the western Pacific in March is much less in JIR P58-78 in comparison to JIR P94-14.

It is necessary to note that the vertical section of potential temperature is warmer up to 3°C in the climatological difference of January OICs (ECMWF ORAS4) between the mean of P58-78 and P94-14 over the

equatorial central and eastern Pacific mainly between 150°W and 100°W at depth from 165 to 70 m (Figures 12a and S17). The Z20 (green line in Figure 12a) in January OICs for P58-78 tends to be deeper in the eastern Pacific in comparison to its locations in January OICs for P94-14 (black line in Figure 12a). The difference of zonal currents between mean of P58-78 and P94-14 in January OICs depicts enhance the magnitude of the EUC in the eastern Pacific (Figure 12b). The magnitude of PT and zonal current in the difference of OICs between mean of P58-78 and P94-14 in April (Figures 12d–12f) is much lower than in January (Figures 12a and 12b). The magnitude of salinity in the difference of OICs between the earlier period and later period is small over the equatorial central Pacific in both January (Figure 12c) and April (Figure 12f) OICs.

The difference between JIR P58-78 and JIR P94-14 displays the large magnitude of subsurface potential temperature and zonal current over the equatorial central and eastern Pacific in the first month of reforecast; one of the possible causes is the larger difference of potential temperature and zonal current in January OICs (ORAS4) between mean of P58-78 and P94-14. As lead months increase (from January to March), the influence of OICs reduces gradually over the equatorial central and eastern Pacific.

The systematic shifts in predicted SST and rainfall during summer over the equatorial Pacific Ocean in the difference between JIR P58-78 and JIR P94-14 is mainly due to a larger magnitude of potential temperature at depth from 165 to 70 m over equatorial central and eastern Pacific and enhance EUC in the eastern Pacific at depth from 125 to 35 m in the OICs of January for period 1958–1978 in comparison to period 1994–2014.

The results of this paper provide the importance of subsurface potential temperature and current conditions in the state-of-the-art CGCM.

Data Availability Statement

I would like to share my data to scientific community that discussed in manuscript through Zenodo (https://doi.org/10.5281/zenodo.3959518) and some large size files are available online (ftp://cola.gmu.edu/pub/ravi/JGROcean2020/ and ftp://cola.gmu.edu/pub/ravi/JGROcean2020.tar). The CFSR was obtained from https://climatedataguide.ucar.edu/climate-data/climate-forecast-system-reanalysis-cfsr website. The global monthly Extended Reconstructed SST, Version 5, was obtained from https://psl.noaa.gov/data/gridded/data.noaa.ersst.v5.html website. Monthly World Ocean Atlas 2009 in situ temperature and salinity was obtained from https://www.nodc.noaa.gov/OC5/WOA09/woa09data.html website.

References

Adams, D. K., & Comrie, A. C. (1997). The North American monsoon. *Bulletin of the American Meteorological Society*, *78*(10), 2197–2213. https://doi.org/10.1175/1520-0477(1997)078%3c2197:TNAM%3e2.0.CO;2

Adler, R. F., Huffman, G. J., Chang, A., Ferraro, R., Xie, P. P., Janowiak, J., et al. (2003). The version-2 Global Precipitation Climatology Project (GPCP) monthly precipitation analysis (1979–present). *Journal of Hydrometeorology*, *4*(6), 1147–1167. https://doi.org/10.1175/1525-7541(2003)004%3c1147:TVGPCP%3e2.0.CO;2

Alexander, M. A., Scott, J. D., & Deser, C. (2000). Processes that influence sea surface temperature and ocean mixed layer depth variability in a coupled model. *Journal of Geophysical Research*, *105*(C7), 16,823–16,842. https://doi.org/10.1029/2000JC900074

Antonov, J. I., Seidov, D., Boyer, T. P., Locarnini, R. A., Mishonov, A. V., Garcia, H. E., et al. (2010). In S. Levitus (Ed.), *World Ocean Atlas 2009, Volume 2: Salinity*, *NOAA Atlas NESDIS 69* (pp. 1–184). Washington, DC: U.S. Government Printing Office.

Balmaseda, M., Vidard, A., & Anderson, D. (2008). The ECMWF System 3 ocean analysis system. *Monthly Weather Review*, *136*(8), 3018–3034. https://doi.org/10.1175/2008MWR2433.1

Balmaseda, M. A., Mogensen, K., & Weaver, A. T. (2013). Evaluation of the ECMWF ocean reanalysis system ORAS4. *Quarterly Journal of the Royal Meteorological Society*, *139*(674), 1132–1161. https://doi.org/10.1002/qj.2063

Battisti, D. S. (1988). Dynamics and thermodynamics of a warming event in a coupled tropical atmosphere–ocean model. *Journal of the Atmospheric Sciences*, *45*(20), 2889–2919. https://doi.org/10.1175/1520-0469(1988)045%3c2889:DATOAW%3e2.0.CO;2

Battisti, D. S., & Hirst, A. C. (1989). Interannual variability in a tropical atmosphere ocean model: Influence of the basic state, ocean geometry and nonlinearity. *Journal of the Atmospheric Sciences*, *46*(12), 1687–1712. https://doi.org/10.1175/1520-0469(1989)046%3c1687:IVIATA%3e2.0.CO;2

Behringer, D. W. (2005). *The global ocean data assimilation system (GODAS) as NCEP*. Paper presented at 11th Symposium on Integrated Observing and Assimilation Systems for the Atmosphere, Oceans, and Land Surface, American Meteorological Society, San Antonio, TX.

Bjerknes, J. (1969). Atmospheric teleconnections from the equatorial Pacific. *Monthly Weather Review*, *97*(3), 163–172. https://doi.org/10.1175/1520-0493(1969)097%3c0163:ATFTEP%3e2.3.CO;2

Cane, M. A., & Zebiak, S. E. (1985). A theory for El Niño and the Southern Oscillation. *Science*, *228*, 1084–1087.

Chowdary, J. S., Parekh, A., Srinivas, G., Gnanaseelan, C., Fousiya, T. S., Khandekar, R., & Roxy, M. K. (2016). Processes associated with the tropical Indian Ocean subsurface temperature bias in a coupled model. *Journal of Physical Oceanography*, *46*(9), 2863–2875. https://doi.org/10.1175/jpo-d-15-0245.1

Deser, C., Capotondi, A., Saravanan, R., & Phillips, A. (2006). Tropical Pacific and Atlantic variability in CCSM3. *Journal of Climate*, *19*(11), 2451–2481. https://doi.org/10.1175/JCLI3759.1

Ek, M. B., Mitchell, K. E., Lin, Y., Rogers, E., Grunmann, P., Koren, V., et al. (2003). Implementation of Noah land surface model advances in the National Centers for Environmental Prediction operational mesoscale Eta model. *Journal of Geophysical Research*, *108*(D22), 8851. https://doi.org/10.1029/2002JD003296

Goswami, B. N., Rao, S. A., Sengupta, D., & Chakravorty, S. (2016). Monsoons to mixing in the Bay of Bengal: Multiscale air-sea interactions and monsoon predictability. *Oceanography*, *29*(2), 18–27. https://doi.org/10.5670/oceanog.2016.35

Griffies, S. M., Harrison, M. J., Pacanowski, R. C., & Rosati, A. (2004). *Technical guide to MOM4, GFDL Ocean Group Technical Report, 5*. Princeton, NJ: Geophysical Fluid Dynamics Laboratory, NOAA. Available at http://www.gfdl.noaa.gov/fms

Higgins, R., Chen, Y., & Douglas, A. (1999). Interannual variability of the North American warm season precipitation regime. *Journal of Climate*, *12*(3), 653–680. https://doi.org/10.1175/1520-0442(1999)012%3c0653:IVOTNA%3e2.0.CO;2

Huang, B., Shin, C. S., Shukla, J., Marx, L., Balmaseda, M., Halder, S., et al. (2017). Reforecasting the ENSO events in the past fifty-seven years (1958–2014). *Journal of Climate*, *30*(19), 7669–7693. https://doi.org/10.1175/JCLI-D-16-0642.1

Huang, B., Thorne, P. W., Banzon, V. F., Boyer, T., Chepurin, G., Lawrimore, J. H., et al. (2017). Extended Reconstructed Sea Surface Temperature version 5 (ERSSTv5), upgrades, validations, and intercomparisons. *Journal of Climate*, *30*(20), 8179–8205. https://doi.org/10.1175/JCLI-D-16-0836.1

Huang, B., Xue, Y., Wang, H., Wang, W., & Kumar, A. (2012). Mixed layer heat budget of the El Niño in NCEP climate forecast system. *Climate Dynamics*, *39*(1–2), 365–381. https://doi.org/10.1007/s00382-011-1111-4

Huang, B., Zhu, J., Marx, L., Wu, X., Kumar, A., Hu, Z. Z., et al. (2015). Climate drift of AMOC, North Atlantic salinity and arctic sea ice in CFSv2 decadal predictions. *Climate Dynamics*, *44*(1–2), 559–583. https://doi.org/10.1007/s00382-014-2395-y

Jin, F.-F. (1997a). An equatorial ocean recharge paradigm for ENSO. Part I: Conceptual model. *Journal of the Atmospheric Sciences*, *54*(7), 811–829. https://doi.org/10.1175/1520-0469(1997)054%3c0811:AEORPF%3e2.0.CO;2

Jin, F.-F. (1997b). An equatorial ocean recharge paradigm for ENSO. Part II: A stripped-down coupled model. *Journal of the Atmospheric Sciences*, *54*(7), 830–847. https://doi.org/10.1175/1520-0469(1997)054%3c0830:AEORPF%3e2.0.CO;2

Johnson, G. C., Sloyan, B. M., Kessler, W. S., & McTaggart, K. E. (2002). Direct measurements of upper ocean currents and water properties across the tropical Pacific during the 1990s. *Progress in Oceanography*, *52*(1), 31–61. https://doi.org/10.1016/s0079-6611(02)00021-6

Kim, H.-M., Webster, P. J., Curry, J. A., & Toma, V. (2012). Asian summer monsoon prediction in ECMWF system 4 and NCEP CFSv2 retrospective seasonal forecasts. *Climate Dynamics*, *39*(12), 2975–2991. https://doi.org/10.1007/s00382-012-1470-5

Kirtman, B. P., & Shukla, J. (2000). Influence of the Indian summer Monsoon on ENSO. *Quarterly Journal of the Royal Meteorological Society*, *126*(562), 213–239. https://doi.org/10.1002/qj.49712656211

Large, W., & Danabasoglu, G. (2006). Attribution and impacts of upper-ocean biases in CCSM3. *Journal of Climate*, *19*(11), 2325–2346. https://doi.org/10.1175/JCLI3740.1

Lau, N. C., & Nath, M. J. (2000). Impact of ENSO on the variability of the Asian-Australian monsoons as simulated in GCM experiments. *Journal of Climate*, *13*(24), 4287–4309. https://doi.org/10.1175/1520-0442(2000)013%3c4287:IOEOTV%3e2.0.CO;2

Locarnini, R. A., Mishonov, A. V., Antonov, J. I., Boyer, T. P., Garcia, H. E., Baranova, O. K., et al. (2010). In S. Levitus (Ed.), *World Ocean Atlas 2009, Volume 1: Temperature*, NOAA Atlas NESDIS 68 (p. 184). Washington, DC: U.S. Government Printing Office.

McPhaden, M. J. (1999). Genesis and evolution of the 1997–98 El Niño. *Science*, *283*(5404), 950–954. https://doi.org/10.1126/science.283.5404.950

McPhaden, M. J. (2004). Evolution of the 2002/03 El Niño. *Bulletin of the American Meteorological Society*, *85*(5), 677–696. https://doi.org/10.1175/BAMS-85-5-677

McPhaden, M. J. (2015). Commentary: Playing hide and seek with El Niño. *Nature Climatic Change*, *5*(9), 791–795.

McPhaden, M. J., Busalacchi, A. J., Cheney, R., Donguy, J. R., Gage, K. S., Halpern, D., et al. (1998). The tropical ocean global atmosphere observing system: A decade of progress. *Journal of Geophysical Research*, *103*(C7), 14,169–14,240. https://doi.org/10.1029/97JC02906

Mogensen, K., Balmaseda, M. A., & Weaver, A. T. (2012). *The NEMOVAR ocean data assimilation system as implemented in the ECMWF ocean analysis for System 4 (ECMWF Tech. Memo. 668)* (pp. 1–61). Reading, UK: European Centre for Medium-Range Weather Forecasts.

Neelin, J. D., Battisti, D. S., Hirst, A. C., Jin, F.-F., Wakata, Y., Yamagata, T., & Zebiak, S. E. (1998). ENSO theory. *Journal of Geophysical Research*, *103*(C7), 14,261–14,290. https://doi.org/10.1029/97JC03424

Pai, D. S., Sridhar, L., Rajeevan, M., Sreejith, O. P., Satbhai, N. S., & Mukhopadyay, B. (2013). *Development and analysis of a new high spatial resolution (0.25 × 0.25) long period (1901–2010) daily gridded rainfall dataset over India* (NCC Reserach Report No. 1/2013, pp. 1–70). Pune, India: India Meteorological Department, National Climate Centre.

Pan, X., Huang, B., & Shukla, J. (2011). Sensitivity of the tropical Pacific seasonal cycle and ENSO to changes in mean state induced by a surface heat flux adjustment in CCSM3. *Climate Dynamics*, *37*(1–2), 325–341. https://doi.org/10.1007/s00382-010-0923-y

Ramu, D. A., Rao, S. A., Pillai, P. A., Pradhan, M., George, G., Rao, D. N., et al. (2017). Prediction of seasonal summer monsoon rainfall over homogenous regions of India using dynamical prediction system. *Journal of Hydrology*, *546*, 103–112. https://doi.org/10.1016/j.jhydrol.2017.01.010

Ramu, D. A., Sabeerali, C. T., Chattopadhyay, R., Rao, D. N., George, G., Dhakate, A. R., et al. (2016). Indian summer monsoon rainfall simulation and prediction skill in the CFSv2 coupled model: Impact of atmospheric horizontal resolution. *Journal of Geophysical Research: Atmospheres*, *121*, 2205–2221. https://doi.org/10.1002/2015JD024629

Rodell, M., Houser, P. R., Jambor, U., Gottschalck, J., Mitchell, K., Meng, C.-J., et al. (2004). The Global Land Data Assimilation System. *Bulletin of the American Meteorological Society*, *85*(3), 381–394. https://doi.org/10.1175/BAMS-85-3-381

Ropelewski, C. F., & Halpert, M. S. (1986). North American precipitation and temperature pattern associated with the El Niño/Southern Oscillation (ENSO). *Monthly Weather Review*, *114*(12), 2352–2362. https://doi.org/10.1175/1520-0493(1986)114%3c2352:NAPATP%3e2.0.CO;2

Rui, H., & Beaudoing, H. (2015). *README document for Global Land Data Assimilation System version 2 (GLDAS-2) products* (pp. 1–23). NASA Goddard Earth Sciences Data and Information Services Center.

Saha, S., Moorthi, S., Pan, H. L., Wu, X., Wang, J., Nadiga, S., et al. (2010). The NCEP climate forecast system reanalysis. *Bulletin of the American Meteorological Society*, *91*(8), 1015–1058. https://doi.org/10.1175/2010BAMS3001.1

Saha, S., Moorthi, S., Wu, X., Wang, J., Nadiga, S., Patrick, T., et al. (2014). The NCEP climate forecast system version 2. *Journal of Climate*, *27*(6), 2185–2208. https://doi.org/10.1175/JCLI-D-12-00823.1

Samanta, D., Hameed, S. N., Jin, D., Thilakan, V., Ganai, M., Rao, S. A., & Deshpande, M. (2018). Impact of a narrow Coastal Bay of Bengal sea surface temperature front on an Indian summer monsoon simulation. *Scientific Reports*, *8*, 17694. https://doi.org/10.1038/s41598-018-35735-3

Schopf, P. F., & Suarez, M. J. (1988). Vacillations in a coupled ocean–atmosphere model. *Journal of the Atmospheric Sciences*, *45*(3), 549–566. https://doi.org/10.1175/1520-0469(1988)045%3c0549:VIACOM%3e2.0.CO;2

Shaji, C., Wang, C., Halliwell, G. R. Jr., & Wallcraft, A. J. (2005). Simulation of tropical Pacific and Atlantic Oceans using a hybrid coordinate ocean model. *Ocean Modelling*, *9*(3), 253–282. https://doi.org/10.1016/j.ocemod.2004.07.003

Shin, C. S., Huang, B., Zhu, J., Marx, L., & Kinter, J. L. (2019). Improved seasonal predictive skill and enhanced predictability of the Asian summer monsoon rainfall following ENSO events in NCEP CFSv2 hindcasts. *Climate Dynamics*, *52*(5–6), 3079–3098. https://doi.org/10.1007/s00382-018-4316-y

Shukla, J., & Paolin, D. A. (1983). The southern oscillation and long range forecasting of the summer monsoon rainfall over India. *Monthly Weather Review*, *11*, 1830–1837.

Shukla, R. P. (2020). Climatological influence of land and atmospheric initial conditions on North America and Eurasia surface temperature and circulation in the past 57 years (1958–2014) reforecasts (under review in the Environmental Research Letters).

Shukla, R. P., & Huang, B. (2015). Mean state and interannual variability of the Indian summer monsoon simulation by NCEP CFSv2. *Climate Dynamics*, *46*(11–12), 3845–3864. https://doi.org/10.1007/s00382-015-2808-6

Shukla, R. P., & Huang, B. (2020). Cumulative influence of summer sub-surface soil temperature on North America surface temperature in NCEP CFSv2. *Journal of Geophysical Research: Atmospheres*, *125*, e2019JD031899. https://doi.org/10.1029/2019JD031899

Shukla, R. P., Huang, B., Dirmeyer, P. A., & Kinter, J. L. (2019). The influence of summer deep soil temperature on early winter snow conditions in Eurasia in the NCEP CFSv2 simulation. *Journal of Geophysical Research: Atmospheres*, *124*, 9062–9077. https://doi.org/10.1029/2019JD030279

Shukla, R. P., Huang, B., Dirmeyer, P. A., Kinter, J. L., Shin, C.-S., & Marx, L. (2019). Climatological Influence of Eurasian winter surface condition on the Asian and Indo-Pacific summer circulation in the CFSv2 Seasonal Reforecasts. *International Journal of Climatology*, *39*(8), 3431–3453. https://doi.org/10.1002/joc.6029

Shukla, R. P., Huang, B., Marx, L., Kinter, J. L., & Shin, C.-S. (2017). Predictability and prediction of Indian summer monsoon by CFSv2: Implication of the initial shock effect. *Climate Dynamics*, *50*(1–2), 159–178. https://doi.org/10.1007/s00382-017-3594-0

Shukla, R. P., & Shin, C.-S. (2020). Distinguishing spread among ensemble members between drought and flood Indian summer monsoon years in the past 58 years (1958–2015) reforecasts. *Geophysical Research Letters*, *47*, e2019GL086586. https://doi.org/10.1029/2019GL086586

Suarez, M. J., & Schopf, P. S. (1988). A delayed action oscillator for ENSO. *Journal of the Atmospheric Sciences*, *45*(21), 3283–3287. https://doi.org/10.1175/1520-0469(1988)045%3c3283:ADAOFE%3e2.0.CO;2

Sun, D.-Z. (2003). A possible effect of an increase in the warm-pool SST on the magnitude of El Niño warming. *Journal of Climate*, *16*(2), 185–205. https://doi.org/10.1175/1520-0442(2003)016%3c0185:APEOAI%3e2.0.CO;2

Towns, J., Cockerill, T., Dahan, M., Foster, I., Gaither, K., Grimshaw, A., et al. (2014). XSEDE: Accelerating scientific discovery. *Computing in Science & Engineering*, *16*(5), 62–74. https://doi.org/10.1109/mcse.2014.80

Uppala, S. M., Kållberg, P. W., Simmons, A. J., Andrae, U., Bechtold, V. D. C., Fiorino, M., et al. (2005). The ERA-40 re-analysis. *Quarterly Journal of the Royal Meteorological Society*, *131*(612), 2961–3012. https://doi.org/10.1256/qj.04.176

Wallace, J. M., Rasmusson, E. M., Mitchell, T. P., Kousky, V. E., Sarachik, E. S., & von Storch, H. (1998). On the structure and evolution of ENSO-related climate variability in the tropical Pacific: Lessons from TOGA. *Journal of Geophysical Research*, *103*(C7), 14,241–14,259. https://doi.org/10.1029/97JC02905

Webster, P. J., & Yang, S. (1992). Monsoon and ENSO: Selectively interactive systems. *Quarterly Journal of the Royal Meteorological Society*, *118*(507), 877–926. https://doi.org/10.1002/qj.49711850705

Winton, M. (2000). A reformulated three-layer sea ice model. *Journal of Atmospheric and Oceanic Technology*, *17*(4), 525–531. https://doi.org/10.1175/1520-0426(2000)017<0525:artlsi>2.0.co;2

Wittenberg, A. T., Rosati, A., Lau, N.-C., & Ploshay, J. J. (2006). GFDL's CM2 global coupled climate models. Part III: Tropical Pacific climate and ENSO. *Journal of Climate*, *19*(5), 698–722. https://doi.org/10.1175/JCLI3631.1

Wyrtki, K. (1975). El-Nino—The dynamic response of the equatorial Pacific Ocean to atmospheric forcing. *Journal of Physical Oceanography*, *5*(4), 572–584. https://doi.org/10.1175/1520-0485(1975)005%3c0572:ENTDRO%3e2.0.CO;2

Wyrtki, K. (1985). Water displacementsin the Pacific and the genesis of E1 Nifio cycles. *Journal of Geophysical Research*, *90*(C4), 7129–7713. https://doi.org/10.1029/JC090iC04p07129

Yeager, S., Christine, A., Large, W., & Hack, J. (2006). The low resolution CCSM3. *Journal of Climate*, *18*, 2545–2566.

Yoo, H., Li, Z., Hou, Y.-T., Lord, S., Weng, F., & Barker, H. W. (2013). Diagnosis and testing of low-level cloud parameterizations for the NCEP/GFS model using satellite and ground-based measurements. *Climate Dynamics*, *41*(5–6), 1595–1613. https://doi.org/10.1007/s00382-013-1884-8

Zhang, T., Sun, D.-Z., Neale, R., & Rasch, P. J. (2009). An evaluation of ENSO asymmetry in the Community Climate System Models: A view from the subsurface. *Journal of Climate*, *22*(22), 5933–5961. https://doi.org/10.1175/2009JCLI2933.1

Zhu, J., Huang, B., Marx, L., Kinter, J. L. III, Balmaseda, M. A., Zhang, R.-H., & Hu, Z.-Z. (2012). Ensemble ENSO hindcasts initialized from multiple ocean analyses. *Geophysical Research Letters*, *39*, L09602. https://doi.org/10.1029/2012GL053053

Zhu, J., & Shukla, J. (2013). The role of air–sea coupling in seasonal prediction of Asia-Pacific summer monsoon rainfall. *Journal of Climate*, *26*(15), 5689–5697. https://doi.org/10.1175/JCLI-D-13-00190.1